



Cite this: *RSC Adv.*, 2023, **13**, 33187

## Facile aqueous synthesis and comparative evaluation of $\text{TiO}_2$ -semiconductor and $\text{TiO}_2$ -metal nanohybrid photocatalysts in antibiotics degradation under visible light<sup>†</sup>

Yuping Zhang,<sup>‡a</sup> Shijie Ju,<sup>‡a</sup> Gregori Casals,<sup>‡b,c</sup> Jie Tang,<sup>a</sup> Yichao Lin,<sup>a</sup> Xiaofang Li,<sup>a</sup> Lihua Liang,<sup>a</sup> Zhiyu Jia,<sup>‡d</sup> Muling Zeng<sup>\*a</sup> and Eudald Casals<sup>‡b</sup>

Advanced oxidation processes using  $\text{TiO}_2$ -based nanomaterials are sustainable technologies that hold great promise for the degradation of many types of pollutants including pharmaceutical residues. A wide variety of heterostructures coupling  $\text{TiO}_2$  with visible-light active nanomaterials have been explored to shift its photocatalytic properties to harness sun irradiation but a systematic comparison between them is lacking in the current literature. Furthermore, the high number of proposed nanostructures with different size, morphology, and surface area, and the often complex synthesis processes hamper the transition of these materials into commercial and effective solutions for environmental remediation. Herein, we have designed a facile and cost-effective method to synthesize two heterostructured photocatalysts representative of two main families of novel structures proposed, hybrids of  $\text{TiO}_2$  with metal (Au) and semiconductor ( $\text{CeO}_2$ ) nanomaterials. The photocatalysts have been extensively characterized to ensure a good comparability in terms of co-catalyst doping characteristics, morphology and surface area. The photocatalytic degradation of ciprofloxacin and sulfamethoxazole as target pollutants, two antibiotics of high concern polluting water sources, has been evaluated and  $\text{CeO}_2/\text{TiO}_2$  exhibited the highest activity, achieving complete antibiotic degradation at very low photocatalyst concentrations. Our study provides new insights into the development of inexpensive heterostructured photocatalysts and suggests that the non-stoichiometry and characteristic d and f electronic orbital configuration of  $\text{CeO}_2$  have a significantly improved role in the enhancement of the photocatalytic reaction.

Received 13th September 2023  
 Accepted 5th November 2023

DOI: 10.1039/d3ra06231g  
[rsc.li/rsc-advances](http://rsc.li/rsc-advances)

### 1. Introduction

Water sources are becoming increasingly scarce due to various factors such as climate change, industrialization, and human activity. Antibiotic abuse and misuse are among the activities particularly detrimental to marine and fluvial ecosystems, and contribute to the development of antibiotic resistance. To address this problem, advanced oxidation processes (AOPs) have been identified as a promising approach to remove water

pollutants, including pharmaceutical residues.<sup>1–4</sup> One widely used AOP is photocatalytic degradation using titanium dioxide ( $\text{TiO}_2$ ) because of its high photocatalytic activity, fast electron transfer ability to molecular oxygen, high stability within a wide pH range, non-toxicity, and low-cost.<sup>5,6</sup> In the catalytic reaction, when  $\text{TiO}_2$  absorbs photons with energies higher or equal to its band gap energy, electrons are promoted from the valence band to the conduction band which generates electron–hole pairs that can oxidize water or hydroxide ions to produce hydroxyl radicals. These radicals act as powerful oxidizing agents.<sup>7</sup> However, the wide band gap of  $\text{TiO}_2$  limits its ability to utilize solar light and the recombination of photo-generated electrons and holes decrease the quantum efficiency.<sup>8</sup> To overcome these limitations, doping  $\text{TiO}_2$  with metal ions such as Cr, V, and Fe was proposed in the 90s, showing a red shift of the band-edge of the  $\text{TiO}_2$ , and this allowed for the catalytic decomposition of NO into  $\text{N}_2$ ,  $\text{O}_2$ , and  $\text{N}_2\text{O}$  under visible light.<sup>9</sup>

With the advent of nanotechnology, the development of heterostructured photocatalysts that involve the coupling of  $\text{TiO}_2$  nanoparticles (NPs) with noble metal NPs (e.g. Pt, Pd and Au)<sup>10–15</sup> or semiconductor NPs (e.g.  $\text{ZnO}$ ,  $\text{Cu}_2\text{O}$ ,  $\text{SnO}_2$ ,  $\text{ZrO}_2$ ,  $\text{WO}_3$ ,

<sup>a</sup>School of Biotechnology and Health Sciences, Wuyi University, Jiangmen 529020, PR China. E-mail: [mulingzeng@163.com](mailto:mulingzeng@163.com); [wyuchemecm@126.com](mailto:wyuchemecm@126.com)

<sup>b</sup>Biochemistry and Molecular Genetics Department, Clinical and Provincial Hospital of Barcelona, Barcelona 08036, Spain

<sup>c</sup>IDIBAPS Research Center, Barcelona 08036, Spain

<sup>d</sup>Key Laboratory of Cluster Science, Ministry of Education of China, Beijing Key Laboratory of Photoelectronic/Electrophotonic Conversion Materials, School of Chemistry and Chemical Engineering, Beijing Institute of Technology, Beijing 100081, PR China. E-mail: [jzy@bit.edu.cn](mailto:jzy@bit.edu.cn)

<sup>†</sup> Electronic supplementary information (ESI) available. See DOI: <https://doi.org/10.1039/d3ra06231g>

<sup>‡</sup> Both authors contributed equally to this study.



and  $\text{CeO}_2$ )<sup>16–21</sup> in different configurations such as core-shells or nanohybrids is an active field of research. These materials are usually chosen for their co-catalyst properties, the plasmonic effect, in the case of metal NPs, which enhances the absorption of light towards the visible range of sunlight, and because they promote the separation of the photoexcited charge carriers (electrons and holes), thus reducing their recombination which prolong the charge separation time and increase redox capacity.<sup>22–25</sup> In a typical report of photocatalytic degradation of pollutants using such NPs, a photocatalyst nanomaterial is proposed and different parameters are explored. For instance, in the case of  $\text{Au}/\text{TiO}_2$ , one of the most widely studied due to the non-toxicity and localized surface plasmon resonance exhibited by AuNPs<sup>12,26–28</sup> it has been shown, among others, how the photocatalytic properties are affected by the interface between Au and  $\text{TiO}_2$ ,<sup>29</sup> the size and shape of Au,<sup>30,31</sup> and the oxidation state of  $\text{TiO}_2$ .<sup>32</sup> In the case of coupling  $\text{TiO}_2$ NPs with other semiconductor NPs,  $\text{TiO}_2/\text{CeO}_2$  hybrid nanostructures are attracting more attention recently due to the improved textural and structural properties of  $\text{TiO}_2$ .<sup>33–36</sup> Different types of  $\text{CeO}_2/\text{TiO}_2$  with different morphologies and textural parameters have been proposed and compared, but a literature review revealed that the preparation conditions of  $\text{TiO}_2/\text{CeO}_2$  have not been investigated in detail to achieve a nanostructure prepared in an industrially feasible way,<sup>37</sup> and this is still a common hindrance for many advanced nanostructures.<sup>38</sup>

Herein, two of the proposed nanostructured  $\text{TiO}_2$ -based photocatalysts have been prepared using simple bench-top chemistry, which are representative of the metal ( $\text{Au}/\text{TiO}_2$ ) and semiconductor ( $\text{CeO}_2/\text{TiO}_2$ ) NP coupling. Furthermore, the photocatalytic degradation using  $\text{Au}/\text{TiO}_2$  and  $\text{CeO}_2/\text{TiO}_2$  of ciprofloxacin (CIP) and sulfamethoxazole (SMX), two of the main antibiotics present in water sources, has been evaluated and compared. CIP is a type of antibiotic belonging to the fluoroquinolone class, commonly used for treating bacterial infections. For instance, in one cluster of Indian pharmaceutical factories consisting of 90 bulk drug manufacturers, the effluent discharge of approximately 1500 m<sup>3</sup> of wastewater per day was found to contain high concentrations of ciprofloxacin, measuring 28 000  $\mu\text{g L}^{-1}$  and 31 000  $\mu\text{g L}^{-1}$  on two consecutive days, exceeding *e.g.* the levels toxic to some bacteria by over 1000-fold.<sup>39</sup> These concentrations correspond to the release of several kilograms of antibiotics daily and tens of tons annually into the environment. Lakes situated in the vicinity of the cluster also showed elevated levels of antibiotic contamination, with ciprofloxacin concentrations measuring up to 6500  $\mu\text{g L}^{-1}$ ,<sup>40</sup> while the Predicted No Effect Concentration-Minimum Inhibitory Concentration (PNEC-MIC) approach described by Bengtsson-Palme and Larsson<sup>41</sup> and the Antimicrobial Resistance Industry Alliance (2018)<sup>42</sup> has been estimated to be 0.064  $\mu\text{g L}^{-1}$ . SMX is a sulfonamide antibiotic that was initially introduced in combination with trimethoprim by F. Hoffmann-La Roche in 1969. Despite a decline in sales figures over the past two decades, SMX continues to be widely utilized, and its PNEC has been estimated to be 0.59  $\mu\text{g L}^{-1}$ .<sup>43,44</sup>

The photocatalysts used in this work have been extensively characterized by a combination of instrumental techniques

including High-Resolution Transmission Electron Microscopy (HR-TEM), X-Ray Diffraction (XRD), UV-VIS spectroscopy, Dynamic Light Scattering (DLS) and BET and X-Ray Photoelectron Spectroscopy (XPS) measurements. Results show that  $\text{CeO}_2/\text{TiO}_2$  exhibit superior photocatalytic performance, achieving complete CIP degradation within 30 and 180 minutes under UV and visible light. Remarkably, coupling  $\text{TiO}_2$ NPs with  $\text{CeO}_2$ NPs also allows the use of the hybrids at lowest reported concentrations, thus reducing the environmental impact of  $\text{TiO}_2$ NPs. The control of single component  $\text{CeO}_2$ NPs also exhibit superior photocatalytic performance in CIP degradation compared to the hybrid  $\text{Au}/\text{TiO}_2$ , which suggest that the inherent redox properties of the co-catalyst  $\text{CeO}_2$  have an important role in the enhancement of the photocatalytic reaction. These results were further confirmed using SMX as pollutant as similar trends were observed.

## 2. Materials and methods

### 2.1. Materials and reagents

All the nanomaterials employed in this work were synthesized in the aqueous phase, using Milli-Q grade water. All reagents were purchased from Sigma-Aldrich (99% purity grade unless indicated otherwise) and used as received. Gold(III) chloride trihydrate ( $\text{HAuCl}_4 \cdot 3\text{H}_2\text{O}$ , CAS No. 16961-25-4) was used as precursor of AuNPs, cerium(III) nitrate hexahydrate ( $\text{Ce}(\text{NO}_3)_3 \cdot 6\text{H}_2\text{O}$ , CAS No. 15878-77-0) as precursor of  $\text{CeO}_2$ NPs and titanium tetrachloride ( $\text{TiCl}_4$ , CAS No. 7550-45-0) as precursor of  $\text{TiO}_2$ NPs. Other reagents utilized for the synthesis of the nanomaterials include sodium borohydride ( $\text{NaBH}_4$ , CAS No. 16940-66-2), trisodium citrate dihydrate (CAS No. 6132-04-3), potassium carbonate ( $\text{K}_2\text{CO}_3$ , CAS No. 584-08-7) and ammonium hydroxide ( $\text{NH}_4\text{OH}$ , 28%  $\text{NH}_3$  in  $\text{H}_2\text{O}$ ,  $\geq 99.99\%$ , CAS No. 1336-21-6). The structure of model antibiotic molecules Ciprofloxacin (CIP) and Sulfamethoxazole (SMX) are illustrated in Fig. S1† and their physio-chemical data listed in Table S1.†

### 2.2. Synthesis of single component Au, $\text{CeO}_2$ and $\text{TiO}_2$ NPs

All the synthesis procedures are based in pre-existed ones available in the scientific literature with few modifications to be adapted for the concentrations needed for this work. AuNPs were synthesized following the procedure based on Jana *et al.*<sup>45</sup> which consist on the fast injection of 0.1 M sodium borohydride (ice-cold freshly prepared) into an aqueous solution containing 0.25 mM Gold(III) chloride trihydrate and 0.25 mM trisodium citrate. This solution was kept under stirring for three hours and stored in the fridge for subsequent experiments.  $\text{CeO}_2$ NPs were synthesized by the chemical precipitation of  $\text{Ce}(\text{NO}_3)_3 \cdot 6\text{H}_2\text{O}$  in a basic aqueous solution following a procedure described in Zeng *et al.*<sup>46</sup> Briefly, 10 mM of  $\text{Ce}(\text{NO}_3)_3 \cdot 6\text{H}_2\text{O}$  was dissolved in 100 mL of Milli-Q water at room temperature. Afterward, 3 mL of 1 M ammonium hydroxide was added slowly at room temperature under vigorous stirring and the mixture was allowed to continue under mild stirring overnight.  $\text{TiO}_2$ NPs synthesis was based in the method described by Pottier *et al.*,<sup>47</sup> the synthesis procedure consists on the decomposition of



titanium tetrachloride ( $TiCl_4$ ) at acidic  $pH = 5$ . Subsequently, the nanocrystals were left to dry in an oven at  $60^\circ C$  for 12 hours and purified by centrifugation steps.

### 2.3. Synthesis of $CeO_2/TiO_2$ and $Au/TiO_2$ hybrid photocatalysts

The hybrid nanostructures were prepared by facile and entirely hydrophilic and open atmosphere synthesis methods. The preparation of  $CeO_2/TiO_2$  involved the following steps: first, 90 mL of the as-prepared  $TiO_2$ NPs ( $5\text{ mg mL}^{-1}$ ) were mixed with 10 mL of  $NH_4OH$  at 75 mM and sonicated during 10 minutes to ensure that  $TiO_2$ NPs were fully dispersed. Second, 108.5 mg of  $Ce(NO_3)_3 \cdot 6H_2O$  were stirred into the mixture and heated under reflux at  $100^\circ C$  for 4 hours. Finally, the resulting solution was washed by purification and colloidally stable  $CeO_2/TiO_2$  were redispersed in a solution of 1 mM  $NH_4OH$ . The preparation of the  $Au/TiO_2$  involved the following steps. First, 96 mL of the as-prepared AuNPs were adjusted to  $pH 10$  by adding equal amounts of sodium citrate and  $K_2CO_3$  at 150 mM. This solution was heated to  $90^\circ C$  under stirring. Second, 4 mL of TTIP (10 mM) was added to the solution and heating was continued for 2 hours. Similar as the  $CeO_2/TiO_2$ , the resulting solution was washed by purification and colloidally stable  $Au/TiO_2$  were redispersed in a solution of 1 mM  $NH_4OH$ .

### 2.4. Characterization techniques

Nanomaterials were visualized using a high-resolution transmission electron microscopy (HR-TEM, FEI Talos, F200s). 40  $\mu\text{L}$  of the colloidal solutions were drop-casted onto a carbon coated 200 mesh copper grid and left to dry at room temperature. Particle size distribution was measured using Image J Analysis software. Hydrodynamic diameters were determined with Dynamic Light Scattering (DLS, Nanotrac wave II, Macchique, USA) with a light source wavelength of 532 nm and fixed scattering angle of  $173^\circ$ . Measurements were conducted in 1 cm path cell and three independent measures were performed. The study of the crystallinity and structural phase of the nanomaterials was performed with a X-ray diffraction (XRD, Rigaku SmartLab SE diffractometer, Tokyo, Japan) using  $Cu K\alpha$  ( $\lambda = 0.15418\text{ nm}$ ) in the range of  $2\theta = 5\text{--}90^\circ$  with an increment of  $0.02^\circ$ . To identify the Ti (2p), O (1s) and Ce (3d) peaks, X-ray photoelectron spectroscopy (XPS) was measured with the Thermo Scientific K-Alpha X-ray photoelectron spectrometer (Thermo Fisher Scientific (China) Co., Ltd.) with  $Al K\alpha$  monochromator as an X-ray source. Nitrogen sorption isotherms were measured with a ASAP2010 analyzer (Micromerites, USA). Before measurements, the samples were dried in a vacuum oven at room temperature for 24 h, and outgassed in the instrument at  $60^\circ C$  for 24 h. The specific surface areas were calculated by the Brunauer–Emmett–Teller (BET) method and the pore size distributions were derived from the adsorption branches of the isotherms using the Barrett–Joiner–Halenda (BJH) method. The optical properties of the photocatalysts were analyzed with UV–Visible Spectrophotometry (UV–VIS), recorded with a Shimadzu UV-1900 (Japan) spectrophotometer. 1 mL of nanomaterials or the solution containing CIP or SMX mixed with the

nanomaterials were added to a quartz cuvette and spectra were achieved with scanning in the wavelength range from 190–700 nm. Table S1† list the characteristics of all nanomaterials employed as described in main text.

### 2.5. Photocatalytic degradation of CIP and SMX

The hybrid and single component nanomaterials were evaluated for the photocatalytic degradation of CIP and SMX both under UV and sunlight. For the degradation experiments under UV light, the artificial irradiation was provided by a 8 W lamp emitting at 365 nm (UV-A) and positioned in top of a quartz reactor (black box, ZF-IB, Shanghai Hannuo Instruments CO., Ltd. Shanghai, China) and maintained at a fixed distance of 5 cm from the samples. The degradation experiments under visible light were carried out at the Wuyi University (Jiangmen, China) whose GPS coordinates are  $22^\circ 35' 53''$  North and  $113^\circ 4' 49''$  East, from 12 p.m. to 4 p.m., 4 h irradiation time and with an average temperature of  $27^\circ C$ . First, the solutions were equilibrated by stirring for 30 minutes in dark condition to achieve adsorption–desorption equilibrium before subjecting them to irradiation. The maintenance of absorbance or a slight decrease in absorbance was observed in some instances at the end of this 30 minute equilibration period, which we refer to as time = 0.<sup>48,49</sup> The experiments were carried out with 10 mL of 10 or 50  $\mu\text{g mL}^{-1}$  of each antibiotic and a optimized concentration of 0.5  $\text{mg mL}^{-1}$  of each photocatalyst. At different time points, the reaction mixtures were centrifuged and the concentration of remaining CIP and SMX in the supernatants were calculated by the maximum absorbance at 272 nm for CIP and 265 nm for SMX. The concentrations of CIP were calculated from a calibration curve using the UV-vis spectroscopy data at a wavelength of 273 nm.

## 3. Results and discussion

### 3.1. Synthesis and characterization of the $CeO_2/TiO_2$ and $Au/TiO_2$ photocatalysts

In a first set of experiments, single component Au,  $CeO_2$ , and  $TiO_2$  NPs were synthesized and further employed for the preparation of the hybrid photocatalysts  $CeO_2/TiO_2$  and  $Au/TiO_2$ , and as controls in the antibiotic degradation experiments. A complete synthesis description and characterization of the single component NPs used in this work can be found in previous publications from the authors<sup>50</sup> and in the materials and methods section. Briefly,  $CeO_2$ NPs were synthesized at room temperature by the precipitation in basic media of  $Ce(NO_3)_3$ ,  $TiO_2$ NPs were prepared following a hydrothermal method based on the decomposition  $TiCl_4$  in acidic media and AuNPs were synthesized by the reduction of  $HAuCl_4$  in the presence of sodium citrate. Fig. S1† shows the Transmission Electron Microscopy (TEM) images of the as-synthesized single-component NPs and their size distributions analysed by TEM and Dynamic Light Scattering (DLS). The mean diameters of  $CeO_2$ ,  $TiO_2$  and Au NPs as determined by TEM image analysis were  $5.4 \pm 1.1\text{ nm}$ ,  $8.6 \pm 2.1\text{ nm}$  and  $8.6 \pm 2.2\text{ nm}$  respectively, and their hydrodynamic diameters was 35.2 nm, 47.7 nm and



14.2 nm with narrow size distributions (polydispersity indexes of 0.1–0.2) as analysed by DLS. The increased hydrodynamic diameter in the case of the metal oxide NPs with respect to the TEM image analysis is attributed to the formation of small agglomerates in solution since the formation of the electrical double layer in metal oxide NPs is less efficient in stabilizing them compared with metal NPs.<sup>51</sup>

The hybrid photocatalysts were prepared by simple wet-chemistry methods. The selection of Au and CeO<sub>2</sub> NPs co-catalyst sizes, ranging between 5 and 10 nanometers, and the loading amount has been made based on their consistent demonstration of enhanced catalytic activity.<sup>52,53</sup> In the case of CeO<sub>2</sub>/TiO<sub>2</sub>, 100 mL of the as-prepared TiO<sub>2</sub>NPs (5 mg mL<sup>-1</sup>) were dispersed in an aqueous ammonia solution of 7.5 mM followed by 10 minutes sonication to disperse the TiO<sub>2</sub>NPs. Afterwards, 108.5 mg of Ce(NO<sub>3</sub>)<sub>3</sub>·6H<sub>2</sub>O were added under stirring to obtain a concentration of Ce<sup>3+</sup> precursor of 2.5 mM. This mixture was heated under reflux and maintained at 100 °C for 4 hours. The synthesis of CeO<sub>2</sub>NPs based on the oxidation of a cerium salt (mainly nitrate or chloride) in basic conditions is common in the literature and it is known that yield monodisperse small-sized (4–5 nm) CeO<sub>2</sub>NPs at this Ce<sup>3+</sup> : NH<sub>4</sub>OH ratio of 1 : 3.<sup>46,54,55</sup> The resulting solution was washed by purification and colloidally stable CeO<sub>2</sub>/TiO<sub>2</sub> were redispersed in a solution of 1 mM TMAOH. Fig. 1a shows TEM and high-angle annular dark field images (HAADF) of the as-synthesized CeO<sub>2</sub>/TiO<sub>2</sub>, which appear as agglomerated nanocomposites containing both CeO<sub>2</sub> and TiO<sub>2</sub>. The HAADF corresponding elemental mapping shows that CeO<sub>2</sub> and TiO<sub>2</sub> NPs are thoroughly distributed in the hybrid structure and the inset reveals the (111) planes of face-centered cubic CeO<sub>2</sub> and (101) of anatase TiO<sub>2</sub>. According to ICP-MS analysis, a 5% of CeO<sub>2</sub> is present in the hybrids, which is consistent with the mass of precursors added in the synthesis. For the Au/TiO<sub>2</sub>, to ensure a good dispersion of the Au and the TiO<sub>2</sub> organized in a similar fashion to the CeO<sub>2</sub>/TiO<sub>2</sub> hybrids, TiO<sub>2</sub>NPs were formed onto previously synthesized AuNPs. 50 mL of the as-prepared AuNPs were adjusted to pH 10 by adding equal amounts of sodium citrate and K<sub>2</sub>CO<sub>3</sub> at 150 mM. The solution was heated to 90 °C under stirring. Subsequently, 50 mL of TiCl<sub>4</sub> (20 mM) was added and the mixture was heated to boiling for 2 hours. As in the case of the CeO<sub>2</sub>/TiO<sub>2</sub> hybrids, the calculated data of 5% of Au in the Au/TiO<sub>2</sub> hybrids is similar than ICP-MS data although slightly increased (7%), probably because not all the TiCl<sub>4</sub> precursor reacted and was washed in the purification step. Fig. 1b shows the TEM and HAADF characterization, where the higher density of metallic Au reveals the dark (bright-field TEM) or white (dark-field TEM) Au nanospheres onto a TiO<sub>2</sub> NPs matrix.

From the TEM images, the presence of both AuNPs and TiO<sub>2</sub>NPs in the Au/TiO<sub>2</sub> hybrids is more clearly evidenced compared with CeO<sub>2</sub>/TiO<sub>2</sub> hybrids thanks to the higher atomic number of Au compared with Ti. Thus, to further prove the presence of CeO<sub>2</sub>NPs and TiO<sub>2</sub>NPs in the CeO<sub>2</sub>/TiO<sub>2</sub> hybrids, the XRD diffraction patterns of the as-synthesized single component CeO<sub>2</sub> and TiO<sub>2</sub> NPs and CeO<sub>2</sub>/TiO<sub>2</sub> hybrid nanostructures were analysed (Fig. 2a and c). The XRD pattern of single component TiO<sub>2</sub>NPs shows the diffraction peaks at 25.3°,

37.9°, 48.0°, 53.9°, 55° and 63°, which can be ascribed to the reflection of (101), (004), (200), (105), (211) and (204) planes of the TiO<sub>2</sub> respectively, consistent with the standard JCPDS values of anatase TiO<sub>2</sub> (JCPDS No. 21-1272). In the case of CeO<sub>2</sub>NPs, the peaks at 28.6°, 33.1°, 47.5°, 56.3° can be ascribed to the (111), (200), (220) and (311) planes of fluorite (cubic) CeO<sub>2</sub> phase (JCPDS No 34-0394). The XRD patterns of both single component NPs exhibit well-defined peaks, although broad due to the small particle size, indicating that the materials are present in a good crystallinity phase. The crystalline sizes of CeO<sub>2</sub>NPs (4.8 nm) and TiO<sub>2</sub>NPs (6.08 nm) calculated from the XRD data using Scherrer's formula (taking the Full Width at Medium Height of the CeO<sub>2</sub> cubic (111) and anatase (101) reflections) are consistent with those obtained by TEM analysis.

In the case of CeO<sub>2</sub>/TiO<sub>2</sub> the calculated crystallite size was 5.12 nm. As the peaks are rather broad, the anatase (101) reflection interfere/mask the CeO<sub>2</sub> cubic (111) main reflection as well as the other dominant (220) and (311) reflections. Other CeO<sub>2</sub> peaks are barely visible due to the low quantity of CeO<sub>2</sub>-NPs in the hybrids. Nonetheless, the smaller crystallite size of the hybrid compared with the pure anatase TiO<sub>2</sub> is attributed to the broadening effect due to the incorporation of CeO<sub>2</sub> into the TiO<sub>2</sub> matrix,<sup>36,56</sup> and it can be noted from the lower intensity and broader width of the peaks of the hybrid compared with pure TiO<sub>2</sub> (Fig. 2c). Furthermore, unshifted peaks of the TiO<sub>2</sub>NPs compared with the CeO<sub>2</sub>/TiO<sub>2</sub> hybrid suggest that the TiO<sub>2</sub> lattices were not disturbed by the presence of Ce ions, probably because of the larger radius of Ce<sup>4+</sup> (0.102 nm) than that of Ti<sup>4+</sup> (0.064 nm) which make it difficult for them to enter into TiO<sub>2</sub> crystal lattice.<sup>57,58</sup> Thus, this suggests that the nanocomposites observed in TEM images are composed of CeO<sub>2</sub> and TiO<sub>2</sub> NPs. In the case of Au/TiO<sub>2</sub> hybrids the presence of the peaks corresponding to Au and TiO<sub>2</sub> can be clearly distinguished and the calculated crystalline size using Scherrer's formula of 6.17 nm was similar to the TiO<sub>2</sub>NPs since the (101) reflection of TiO<sub>2</sub> is not affected by the presence of the AuNPs (Fig. S2†).

Additionally, Raman spectra were employed to further confirm the above description in the case of CeO<sub>2</sub>/TiO<sub>2</sub> (Fig. 2b). Single component TiO<sub>2</sub>NPs and TiO<sub>2</sub>/CeO<sub>2</sub> hybrids show the characteristic Raman-active modes of TiO<sub>2</sub> anatase phase (A<sub>1g</sub>, B<sub>1g</sub>, E<sub>g</sub>) which are ascribed to the 145, 196, 397, 517 and 639 cm<sup>-1</sup> peaks.<sup>59</sup> As in the case of XRD, the peak of CeO<sub>2</sub>NPs (464 cm<sup>-1</sup>) is barely noted in the CeO<sub>2</sub>/TiO<sub>2</sub>, but, it can be noted the broadening and blue shift of the most intense peak in the hybrid respect with TiO<sub>2</sub>NPs. This has been attributed to non-stoichiometric defects and non-homogeneity of particle size distribution due to the presence of the CeO<sub>2</sub>NPs,<sup>36,60</sup> which is consistent with the XRD results.

Further, X-ray photoelectron spectroscopy (XPS) was employed to analyse the chemical composition and chemical state of elements in the CeO<sub>2</sub>/TiO<sub>2</sub> hybrids. Fig. 2d-g shows the high-resolution XPS spectra of Ti 2p, Ce 3d, and O 1s in the CeO<sub>2</sub>/TiO<sub>2</sub>. In the survey plot (Fig. 2d) the presence of four main elements Ti, O, Ce, and C can be observed. The presence of C is common in XPS analysis due to contamination from environmental air during sample preparation. The peaks at 530 and 532 eV are assigned to O<sup>2-</sup> ion in the TiO<sub>2</sub> crystal structure and



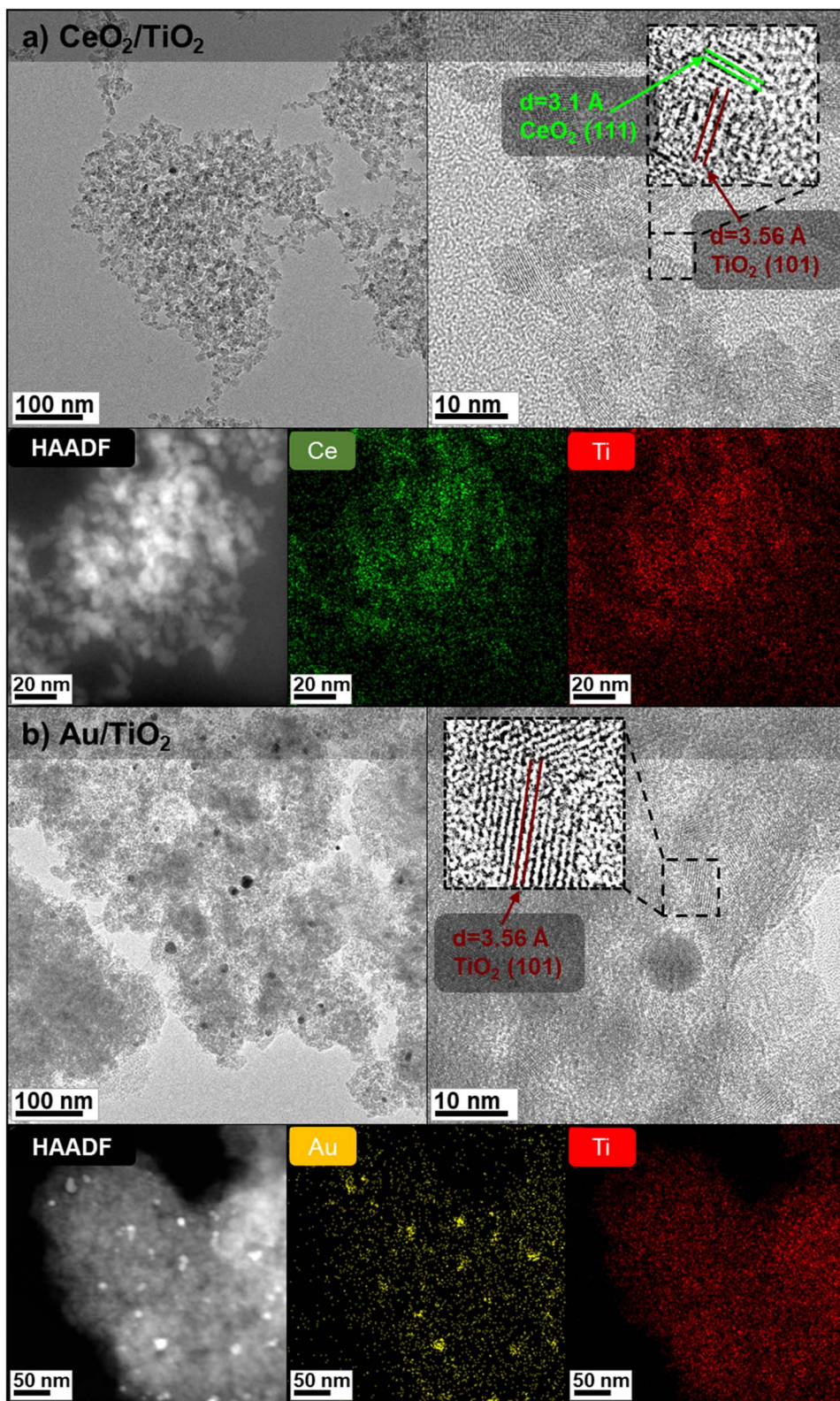
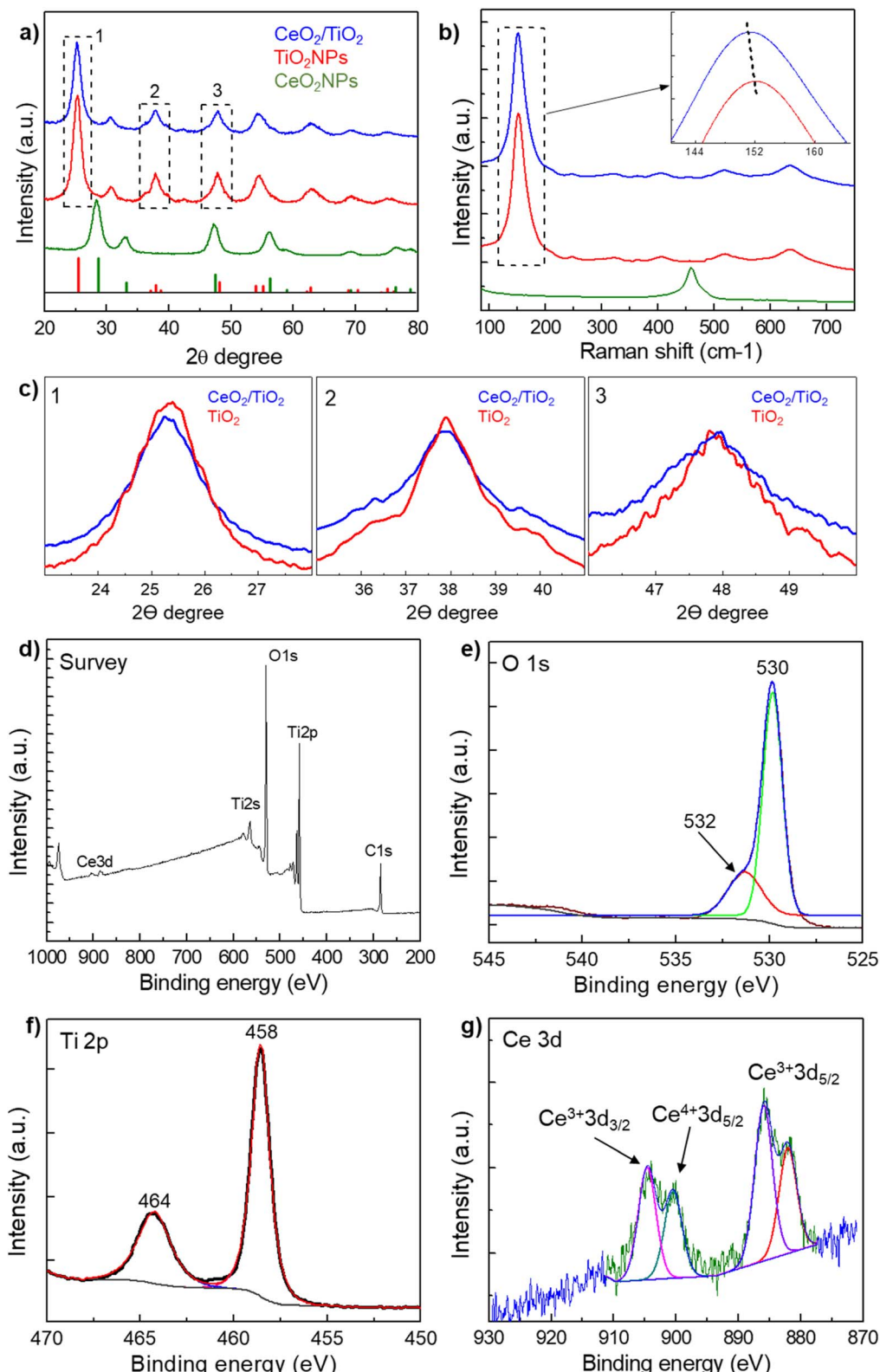


Fig. 1 Morphology of the  $\text{CeO}_2/\text{TiO}_2$  (a) and  $\text{Au}/\text{TiO}_2$  (b) hybrid nanostructures. For each hybrid, upper rows show representative TEM images and lower rows the high-angle annular dark field TEM (HAADF-TEM) images revealing the formation of both  $\text{CeO}_2$  and  $\text{TiO}_2$  in the  $\text{CeO}_2/\text{TiO}_2$  and  $\text{Au}$  and  $\text{TiO}_2$  in the  $\text{Au}/\text{TiO}_2$ . Inset in (a) shows the (111) planes of face-centered cubic  $\text{CeO}_2$  phase and (101) of anatase  $\text{TiO}_2$  and inset in (b) the (101) of anatase  $\text{TiO}_2$ .



**Fig. 2** Physicochemical characterization of the  $\text{CeO}_2/\text{TiO}_2$  hybrid nanostructures. (a) XRD patterns of the  $\text{CeO}_2$  and  $\text{TiO}_2$  NPs and the  $\text{CeO}_2/\text{TiO}_2$  hybrid. (b) Raman spectra of the  $\text{CeO}_2$  and  $\text{TiO}_2$  NPs and the  $\text{CeO}_2/\text{TiO}_2$  hybrid. Inset is the predominant peak of  $\text{TiO}_2$  which is blue-shifted in the  $\text{CeO}_2/\text{TiO}_2$  hybrid. (c) Details of the anatase  $\text{TiO}_2$  and  $\text{CeO}_2/\text{TiO}_2$  hybrid diffraction peaks at around  $25^\circ$  (1),  $38^\circ$  (2) and  $48.0^\circ$  (3). (d–g) XPS analysis of the  $\text{CeO}_2/\text{TiO}_2$  including survey spectra (d), O 1s core-level spectra (e), Ti 2p core-level spectra (f) and Ce 3d core-level spectra (g).

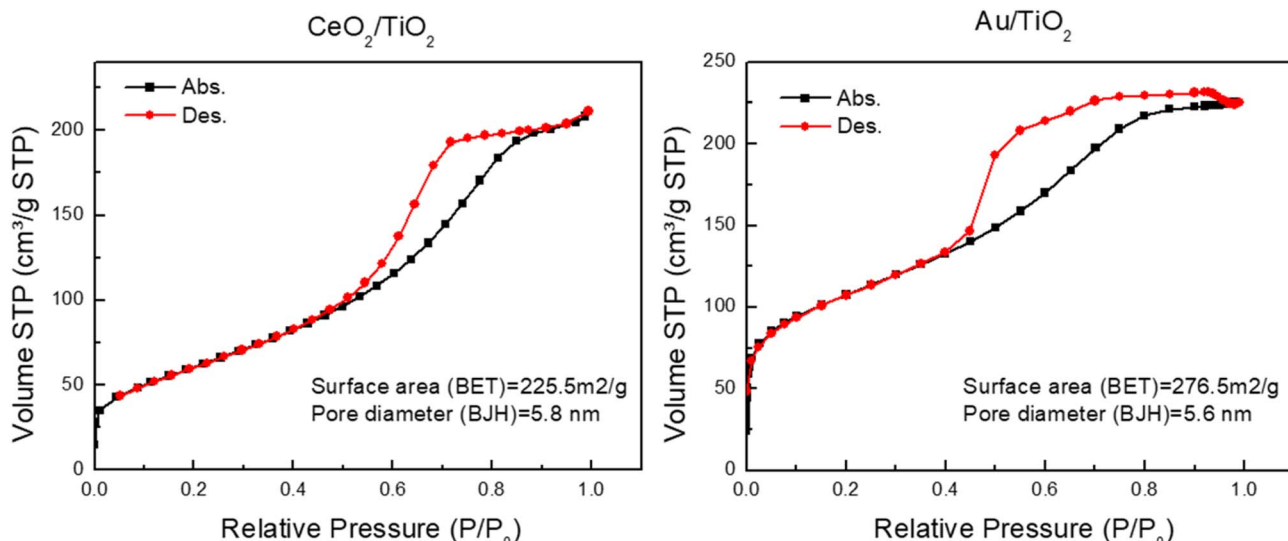


Fig. 3 Nitrogen sorption isotherms and textural properties of the  $\text{CeO}_2/\text{TiO}_2$  (left) and the  $\text{Au}/\text{TiO}_2$  (right) hybrid nanostructures.

Ti-OH bond (Fig. 2e). The dominant peak located at 530 eV has been described as characteristic of metal oxides arising from the lattice of  $\text{CeO}_2$  and  $\text{TiO}_2$ .<sup>61</sup> The Ti 2p core-level spectrum (Fig. 2f) shows two major peaks at 458.4 and 464.2 eV, corresponding to the Ti 2p<sub>3/2</sub> and Ti 2p<sub>1/2</sub> spin-orbit split photoelectrons of  $\text{Ti}^{4+}$  respectively, which is characteristic of  $\text{TiO}_2$  species. In the case of Ce, the 4f group is particularly complex because of its associated peak structure. The Ce3d core-level spectrum (Fig. 2g) shows different groups of peaks. One group of two peaks at 882 eV corresponds to the  $\text{Ce}^{3+}$  3d<sub>5/2</sub> spin orbital and another group of two peaks around 900 eV corresponds to the  $\text{Ce}^{4+}$  3d<sub>5/2</sub> (898 eV) and  $\text{Ce}^{3+}$  3d<sub>3/2</sub> (904 eV).<sup>62,63</sup> In both cases, the peaks are asymmetric, which is attributed to the mixture of  $\text{Ce}^{3+}$  and  $\text{Ce}^{4+}$  in the  $\text{CeO}_2$  NPs structure.<sup>57,64-66</sup> Furthermore, based on the non-linear least squares fitting of  $\text{CeO}_2$  synthesized as in the hybrids, composition of  $\text{Ce}^{3+}$  and  $\text{Ce}^{4+}$  were found to be 65.1% and 34.9% respectively. The presence of both  $\text{Ce}^{4+}$  and  $\text{Ce}^{3+}$  in the  $\text{CeO}_2$  from the  $\text{CeO}_2/\text{TiO}_2$  hybrids is important since it improves the electron transfer characteristics and the separation efficiency of photogenerated electrons and holes, and consequently it is expected it will improve the photocatalytic activity with respect to pure  $\text{TiO}_2$ .

Finally, nitrogen adsorption/desorption measurements were performed on the  $\text{CeO}_2/\text{TiO}_2$  and  $\text{Au}/\text{TiO}_2$  hybrid nanostructures to determine their specific surface area and textural properties. Fig. 3 displays the isotherms, revealing that both photocatalysts exhibited a characteristic type-IV isotherm, as per the IUPAC classification. This observation indicates a well-developed mesoporous structure. The BET surface area and average pore diameter determined from the adsorption branch using the BJH method for  $\text{CeO}_2/\text{TiO}_2$  were  $225.5 \text{ m}^2 \text{ g}^{-1}$  and 5.8 nm, respectively. Meanwhile, for  $\text{Au}/\text{TiO}_2$ , these values were  $276.9 \text{ m}^2 \text{ g}^{-1}$  and 5.6 nm. This suggests that the obtained hybrids share similar characteristics, not only in terms of size and co-catalyst doping but also in morphology and surface area and that the coupling of  $\text{CeO}_2$  or  $\text{Au}$  NP lead to similar hybrid structures.

### 3.2. Optical properties of the $\text{CeO}_2/\text{TiO}_2$ and $\text{Au}/\text{TiO}_2$ photocatalysts

The optical properties of both  $\text{CeO}_2/\text{TiO}_2$  and  $\text{Au}/\text{TiO}_2$  were investigated by UV/VIS spectroscopy. Fig. 4a shows the UV/VIS spectra for both  $\text{CeO}_2/\text{TiO}_2$  and  $\text{Au}/\text{TiO}_2$ , along with the single component NPs, which confirm the presence of the single component NPs in both hybrids. Furthermore, it can be observed that compared with pure  $\text{TiO}_2$ , both hybrid structures display an extension of their UV/VIS absorbance to the visible light region. Next, the band gap energy ( $E_g$ ) values of the single component and hybrid nanostructures were determined by fitting the UV/VIS data with Tauc's plots<sup>67,68</sup> following the developments by Davis and Mott for amorphous semiconductors,<sup>69</sup> and later by many others. It is worth noting that the linear extrapolation to zero in the plots of  $(\alpha h\nu)^2$  versus photon energy to estimate  $E_g$  values, is a common approach for providing a rough approximation of the direct band gap. This is because the Tauc plot method assumes measurements under specific conditions, potentially introducing uncertainties.<sup>70</sup> Additionally, variations in the data or the choice of the linear fitting range can impact the accuracy of the estimated bandgap. The  $E_g$  values for  $\text{TiO}_2$ ,  $\text{CeO}_2$ ,  $\text{Au}/\text{TiO}_2$  and  $\text{CeO}_2/\text{TiO}_2$  are 3.52, 3.55, 3.34 and 3.01 eV respectively (Fig. 4b). The  $E_g$  is lower in the hybrids compared with the single component NPs which confirms again the incorporation of both  $\text{Au}$  and  $\text{CeO}_2$  in the  $\text{TiO}_2$  matrix to form the hybrid nanostructures.

Importantly, the decrease of  $E_g$  values in the hybrids compared with  $\text{TiO}_2$  NPs is an indication of the red shifting from UV to the visible region. Therefore, it can be hypothesized that this will enable the photocatalytic activity under sun irradiation. This can be explained by the electronic band structure in the hybrids.  $\text{CeO}_2$  is a p-type semiconducting photocatalyst material with potentially suitable band positions for the promotion of charge carriers when kept in intimate connection with  $\text{TiO}_2$ . When electrons in the  $\text{CeO}_2$  valence band are exposed to lower energy lights (e.g. visible light) they move to the conduction



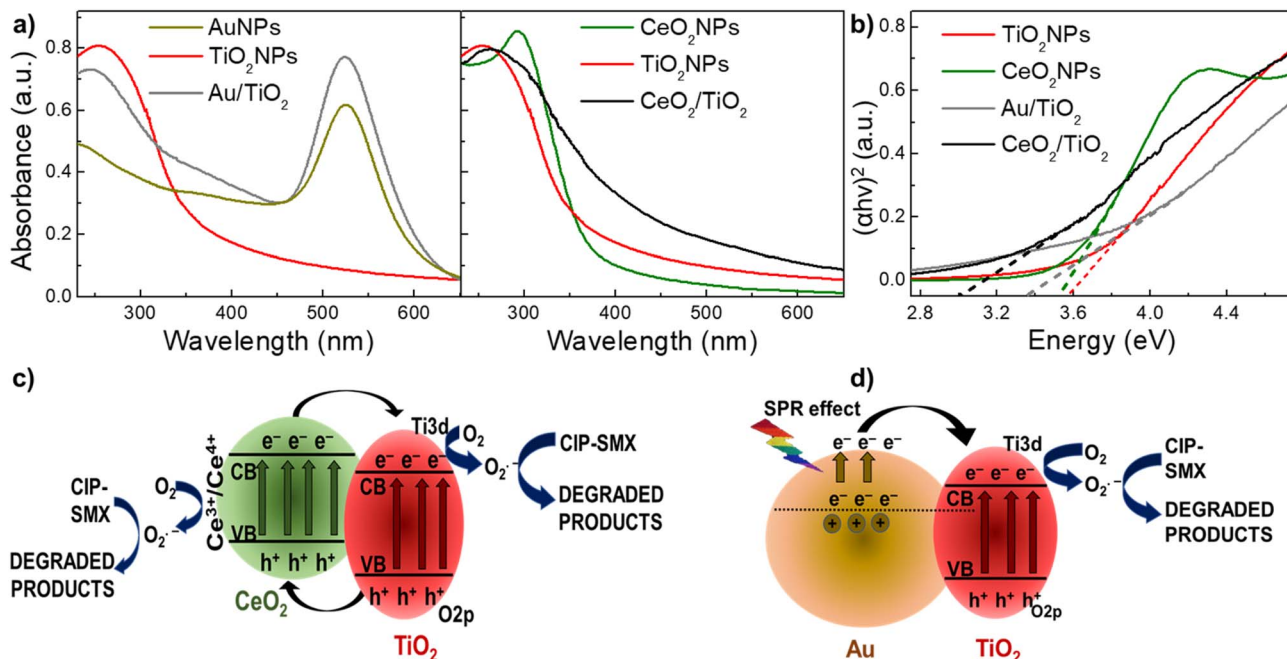


**Fig. 4** Optical properties of the CeO<sub>2</sub>/TiO<sub>2</sub> and Au/TiO<sub>2</sub> hybrid nanostructures. (a) UV/VIS spectra of both hybrids along with the single component NPs. (b) Corresponding Tauc plots which represent the square of the absorption coefficient versus photon energy. The bandgap energy ( $E_g$ ) of the material can be determined from the x-axis intercept of the linear portion of the curve. (c and d) Schematic diagram of the proposed mechanism for the photocatalysis by CeO<sub>2</sub>/TiO<sub>2</sub> (c) and Au/TiO<sub>2</sub> (d) under visible light irradiation. The different band structures of the co-catalysts respect TiO<sub>2</sub> facilitate the transfer of electrons to the TiO<sub>2</sub> conduction band (CB), and subsequently from the CB of TiO<sub>2</sub> to oxygen molecules, resulting in the formation of superoxide radicals (O<sup>2-</sup>). Furthermore, the co-catalysts facilitate the regeneration of the CB of TiO<sub>2</sub> and act as a trap for the photo-generated holes, preventing their recombination with electrons and prolonging the lifetime of the charge carriers, thus potentially enhancing the photocatalytic activity. Additionally, CeO<sub>2</sub>NPs can undergo oxidation reactions by themselves.

band. As a result of the varied energy barriers of both components in the hybrids, electrons will eventually relocate to the conduction band of TiO<sub>2</sub>.<sup>36,71</sup> Further, electrons in the TiO<sub>2</sub> valence band will also undergo excitation when exposed to higher energy light (e.g. UV which accounts for the 4% of the sun irradiation), and the hole in its valence band will shift to the CeO<sub>2</sub> valence band. This carrier transport process efficiently separates photoelectrons and holes, making their recombination more difficult and broadening the response to visible light.<sup>71</sup> Au/TiO<sub>2</sub> is most well-described in the literature. In such nanostructures, due to SPR in the Au surface, electrons from the AuNPs conduction band become excited (known as hot electrons) under visible light irradiation. These charge carriers are relocated from the excited AuNPs to the conduction band of the adjacent TiO<sub>2</sub>, since there is close contact between the surfaces of Au and TiO<sub>2</sub> (known as Schottky junction). This movement generates holes in the AuNPs electronic structure and achieves a similar effect as described in the CeO<sub>2</sub>/TiO<sub>2</sub>, making electron-hole recombination more difficult. Thus, with the efficient supply of hot electrons TiO<sub>2</sub> can undergo the photocatalytic reaction under light illumination.<sup>12,27,28,72</sup> Fig. 4c and d shows a scheme of these carrier transport processes under visible light of CeO<sub>2</sub>/TiO<sub>2</sub> and Au/TiO<sub>2</sub> hybrid nanostructures.

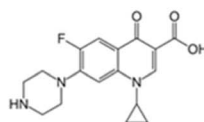
### 3.3. Degradation of CIP and SMX

All material improvements of the Au/TiO<sub>2</sub> and CeO<sub>2</sub>/TiO<sub>2</sub> hybrids described in the previous sections compared with the

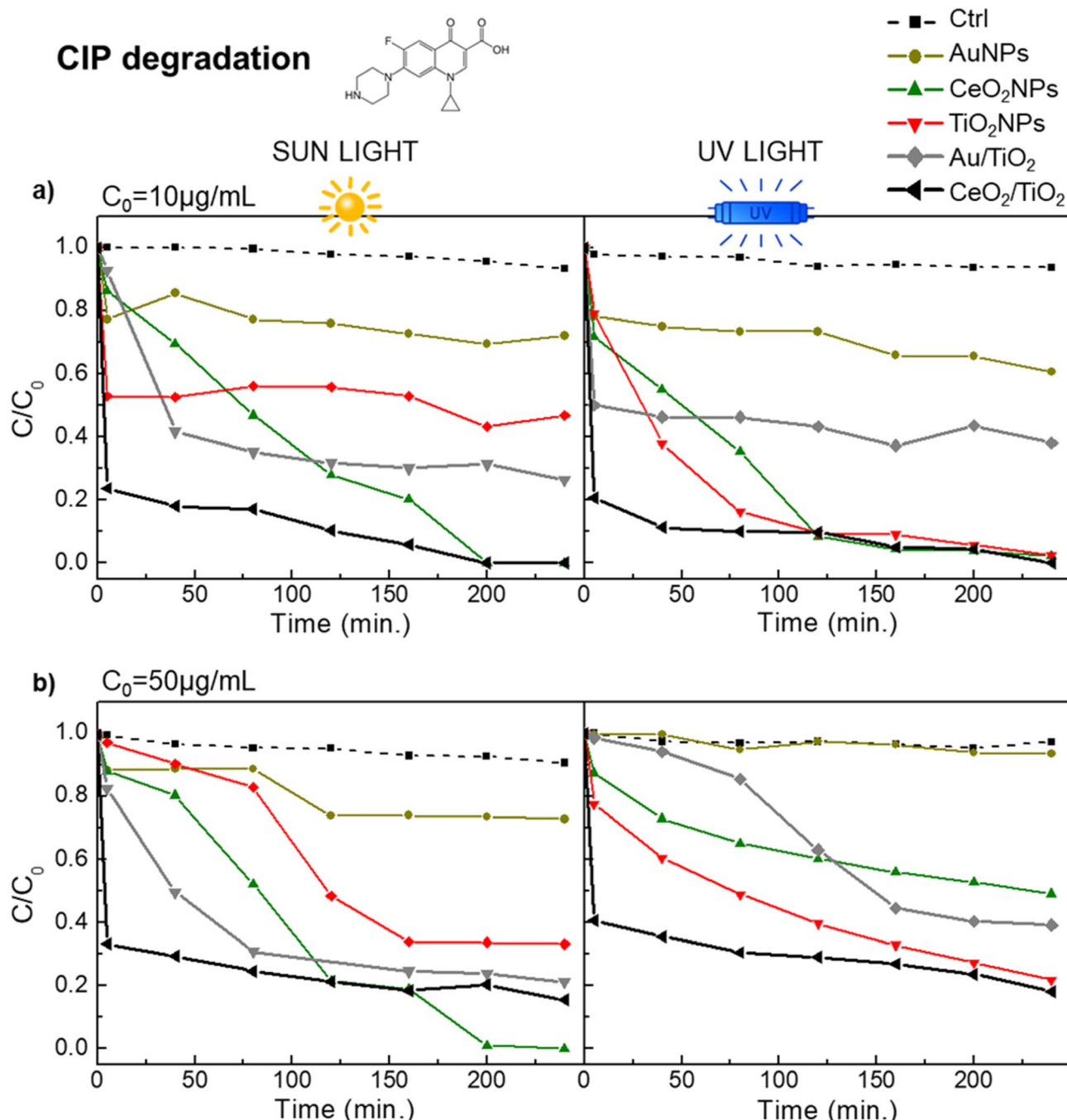
single component NPs were evaluated and compared in the context of CIP and SMX degradation. First, the concentration of the photocatalysts to be used in the degradation experiments was determined. This is important since increasing the concentration of a photocatalyst can increase its photocatalytic activity up to a point where the solution becomes turbid due to a high concentration of particles, which reduces the penetration of the light (effect known as catalyst shielding). In addition, the high catalyst concentration may also block access to the catalytic sites because of the agglomeration of the particles. The effect of catalyst concentration on the degradation of Rhodamine B (RhB) and CIP with TiO<sub>2</sub>NPs was studied. First, varying concentration of TiO<sub>2</sub>NPs were used for the degradation of RhB at initial concentration of 2.5 mM (Fig. S3†). From these studies, 0.5 mg mL<sup>-1</sup> of photocatalyst was selected as optimized concentration, which is a similar result than the previously reported for TiO<sub>2</sub> and Au/TiO<sub>2</sub> for RhB degradation.<sup>72,73</sup> Next, we used 0.5 mg mL<sup>-1</sup> of CeO<sub>2</sub>/TiO<sub>2</sub> and Au/TiO<sub>2</sub> hybrids (and TiO<sub>2</sub>, CeO<sub>2</sub> and Au single component NPs as controls) to corroborate its suitability for the degradation of 10 µg L<sup>-1</sup> of CIP.

Fig. 5a shows the kinetic plots of CIP degradation, where CeO<sub>2</sub>, TiO<sub>2</sub> and the CeO<sub>2</sub>/TiO<sub>2</sub> hybrids showed 100% CIP degradation (although at different time points in each case). This concentration of photocatalysts was used with further experiments under sun irradiation (Fig. 5a) and with an increased CIP concentration of 50 µg L<sup>-1</sup> (Fig. 5b). The CIP<sup>48,74</sup> and SMX<sup>75,76</sup> degradation pathways and degraded products





## CIP degradation



**Fig. 5** Photocatalytic performance in the degradation of CIP of the hybrid  $\text{CeO}_2/\text{TiO}_2$ ,  $\text{Au}/\text{TiO}_2$  and single component NPs under visible and UV light. (a) CIP initial concentration of  $10 \mu\text{g mL}^{-1}$ ; (b) CIP initial concentration of  $50 \mu\text{g mL}^{-1}$  (b). Black and grey line correspond to  $\text{CeO}_2/\text{TiO}_2$  and  $\text{Au}/\text{TiO}_2$  hybrids respectively. Yellow line is AuNPs, green line is  $\text{CeO}_2$ NPs, red line is  $\text{TiO}_2$  NPs and dashed line correspond to the control ( $\text{H}_2\text{O}$ ). All photocatalysts were used at a concentration of  $0.5 \text{ mg mL}^{-1}$ . The control group (ctrl) consists of the antibiotic dissolved in a water solvent. The molecular structure of CIP is in Fig. S1.†

using  $\text{TiO}_2$ NPs and hybrid  $\text{TiO}_2$ -based photocatalysts both under UV and sun irradiation have been reported elsewhere, as well as the toxicity of the resulting degradation products. For instance, in the case of CIP, Durán-Álvarez *et al.*<sup>77</sup> reported negligible toxicity towards *Vibrio fischeri* and the complete removal of antibiotic activity against *Escherichia coli* when employing  $\text{TiO}_2$  modified with metallic NPs at an initial CIP

concentration of  $30 \mu\text{g mL}^{-1}$ . This was attributed to the complete mineralization of CIP following 360 minutes of photocatalytic treatment under simulated sunlight irradiation. Similarly, Zheng *et al.*<sup>78</sup> obtained comparable results using  $\text{TiO}_2$ -based nanocomposites at an initial CIP concentration of  $30 \mu\text{g mL}^{-1}$ . Regarding SMX, among others, Borowska *et al.*<sup>76</sup> reported the decrease of phytotoxicity of SMX degraded

**Table 1** Degradation of CIP and SMX (%) using the synthesized photocatalysts at 0.5 mg mL<sup>-1</sup>

	CIP degradation (%)				SMX degradation (%)			
	$C_0$ (CIP)		$C_0$ (CIP)		$C_0$ (SMX)		$C_0$ (SMX)	
	10 $\mu\text{g mL}^{-1}$	50 $\mu\text{g mL}^{-1}$	5 $\mu\text{g mL}^{-1}$	10 $\mu\text{g mL}^{-1}$	SUN	UV	SUN	UV
	AuNPs	27.8	39.4	27.2	65.2	21.7	20.3	25.4
CeO <sub>2</sub> NPs	99.9	97.8	99.9	50.9	69.5	40.6	78.8	23.8
TiO <sub>2</sub> NPs	53.2	97.5	66.8	78.2	34.6	65.1	29.4	66.1
Au/TiO <sub>2</sub>	73.7	61.9	78.8	60.9	56.7	42.2	49.2	32.8
CeO <sub>2</sub> /TiO <sub>2</sub>	99.9	99.9	84.6	81.8	87.7	84.2	67.7	32.5

products towards the plant *Lepidium sativum* when using TiO<sub>2</sub>NPs doped with noble metals at an initial SMX concentration of 1  $\mu\text{g mL}^{-1}$ . This low phytotoxicity was attributed to the very low concentrations of remaining antibiotics. Gong *et al.*<sup>79</sup> also observed a significant reduction in toxic activity against the green alga *Chlorella vulgaris* and the brine shrimp *Artemia salina* after photodegradation of SMX under UV radiation.

In all cases, a similar pattern can be observed. CeO<sub>2</sub>/TiO<sub>2</sub> hybrids consistently show the highest CIP degradation rate compared to the other nanomaterials. Specifically, at a CIP concentration of 10  $\mu\text{g L}^{-1}$ , both CeO<sub>2</sub>/TiO<sub>2</sub> and CeO<sub>2</sub>NPs showed complete degradation under UV and sun irradiation while TiO<sub>2</sub>NPs show 100% degradation under UV light and 50%

degradation under sun irradiation. In the case of the CeO<sub>2</sub>/TiO<sub>2</sub> hybrids, the degradation was found to be constant after 40 min of reaction time, while for other nanomaterials it took around 2 hours to reach the stability, suggesting a more powerful activity of the CeO<sub>2</sub>/TiO<sub>2</sub> in all conditions. As expected, Au/TiO<sub>2</sub> hybrids also enhanced the photocatalytic activity of TiO<sub>2</sub> under sun irradiation, although to a lesser extent than CeO<sub>2</sub>/TiO<sub>2</sub> (around 75% CIP degradation in the case of Au/TiO<sub>2</sub> while 50% degradation was observed in the case of TiO<sub>2</sub> at an initial concentration of CIP of 10  $\mu\text{g mL}^{-1}$ ), and AuNPs showed less than 20% CIP degradation in those conditions. Table 1 shows the percentage of CIP degradation in all cases.

Remarkably, the amount of photocatalyst used was lower than many other studies also aimed to study the degradation of CIP by nanostructured photocatalysts. Among others (see Table 2 for full list), Manasa *et al.*<sup>48</sup> employing 1 mg mL<sup>-1</sup> of Ce-doped TiO<sub>2</sub>NPs achieved 93% CIP degradation at  $C_0 = 10 \mu\text{g mL}^{-1}$ . Pattnaik *et al.*<sup>80</sup> employing exfoliated graphitic carbon nitride (g-C<sub>3</sub>N<sub>4</sub>) found that the same 1 mg mL<sup>-1</sup> concentration of photocatalyst degraded up to 78% of a 20  $\mu\text{g mL}^{-1}$  CIP solution exposed to solar light. Yu *et al.*<sup>81</sup> employing Zn-doped Cu<sub>2</sub>ONPs at 0.6 mg mL<sup>-1</sup> achieved 94.6 CIP degradation at  $C_0 = 20 \mu\text{g mL}^{-1}$ . Furthermore, Gad-Allah *et al.*<sup>82</sup> used 1.5 mg mL<sup>-1</sup> of TiO<sub>2</sub>NPs to efficiently degrade CIP at  $C_0 = 50 \mu\text{g mL}^{-1}$ , in this case using simulated sunlight.

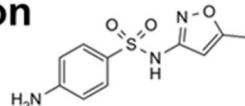
These results were further corroborated with the photocatalytic degradation of SMX in the same conditions as the used

**Table 2** Degradation of CIP by different nanostructured photocatalysts under visible light

	Concentration of photocatalyst (mg mL <sup>-1</sup> )	CIP initial concentration ( $\mu\text{g mL}^{-1}$ )	CIP degradation
<b>TiO<sub>2</sub>-based photocatalysts</b>			
TiO <sub>2</sub> NPs (under simulated sunlight) <sup>82</sup>	1.5 mg mL <sup>-1</sup>	50 $\mu\text{g mL}^{-1}$	99.9%
P25-TiO <sub>2</sub> (ref. 83)	1 mg mL <sup>-1</sup>	20 $\mu\text{g mL}^{-1}$	31%
P25-TiO <sub>2</sub> (ref. 84)	1.5–11 mg mL <sup>-1</sup>	30 $\mu\text{g mL}^{-1}$	99%
Immobilized TiO <sub>2</sub> NPs <sup>85</sup>	1 mg mL <sup>-1</sup>	3 $\mu\text{g mL}^{-1}$	92.8%
Immobilized TiO <sub>2</sub> NPs <sup>86</sup>	7.5 mg mL <sup>-1</sup>	20 $\mu\text{g mL}^{-1}$	95%
Au-TiO <sub>2</sub> , Ag-TiO <sub>2</sub> and Cu-TiO <sub>2</sub> (ref. 77)	1.5 mg mL <sup>-1</sup>	30 $\mu\text{g mL}^{-1}$	99%
Hybrid TiO <sub>2</sub> :Au nanostars <sup>87</sup>	1 mg mL <sup>-1</sup>	5 $\mu\text{g mL}^{-1}$	89%
Ce-doped TiO <sub>2</sub> (ref. 48)	1 mg mL <sup>-1</sup>	10 $\mu\text{g mL}^{-1}$	93%
g-C <sub>3</sub> N <sub>4</sub> /TiO <sub>2</sub> powder <sup>49</sup>	1 mg mL <sup>-1</sup>	10 $\mu\text{g mL}^{-1}$	95%
Chlorophyll sensitized TiO <sub>2</sub> NPs <sup>88</sup>	0.75 mg mL <sup>-1</sup>	10 $\mu\text{g mL}^{-1}$	75%
<b>Other materials</b>			
MnO <sub>2</sub> (ref. 89)	7 mg mL <sup>-1</sup>	10 $\mu\text{g mL}^{-1}$	90%
		20 $\mu\text{g mL}^{-1}$	60%
Pt/InVO <sub>4</sub>	3 mg mL <sup>-1</sup>	20 $\mu\text{g mL}^{-1}$	87%
Pt-BiVO <sub>4</sub> (ref. 90)	1.5 mg mL <sup>-1</sup>	10 $\mu\text{g mL}^{-1}$	92%
Exfoliated g-C <sub>3</sub> N <sub>4</sub> (ref. 80)	1 mg mL <sup>-1</sup>	20 $\mu\text{g mL}^{-1}$	78%
Zn-doped Cu <sub>2</sub> O <sup>81</sup>	0.6 mg mL <sup>-1</sup>	20 $\mu\text{g mL}^{-1}$	94.6%
N-ZnO/CdS/GO <sup>91</sup>	0.5 mg mL <sup>-1</sup>	15 $\mu\text{g mL}^{-1}$	85%
CeO <sub>2</sub> /CdS/RGO <sup>92</sup>	0.5 mg mL <sup>-1</sup>	40 $\mu\text{g mL}^{-1}$	90%
N doped-graphene quantum dots-BiVO <sub>4</sub> /gC <sub>3</sub> N <sub>4</sub> (ref. 93)	0.5 mg mL <sup>-1</sup>	10 $\mu\text{g mL}^{-1}$	72%
CeO <sub>2</sub> /ZnO nanocomposites <sup>94</sup>	0.25 mg mL <sup>-1</sup>	15 $\mu\text{g mL}^{-1}$	60%
Reduced graphene oxide-BiVO <sub>4</sub> (ref. 95)	0.2 mg mL <sup>-1</sup>	10 $\mu\text{g mL}^{-1}$	68.2%
<b>This study</b>			
CeO <sub>2</sub> -TiO <sub>2</sub>	0.5 mg mL <sup>-1</sup>	10 $\mu\text{g mL}^{-1}$	99.9%
CeO <sub>2</sub> -TiO <sub>2</sub>	0.5 mg mL <sup>-1</sup>	50 $\mu\text{g mL}^{-1}$	85%



## SMX degradation



SUN LIGHT

UV LIGHT

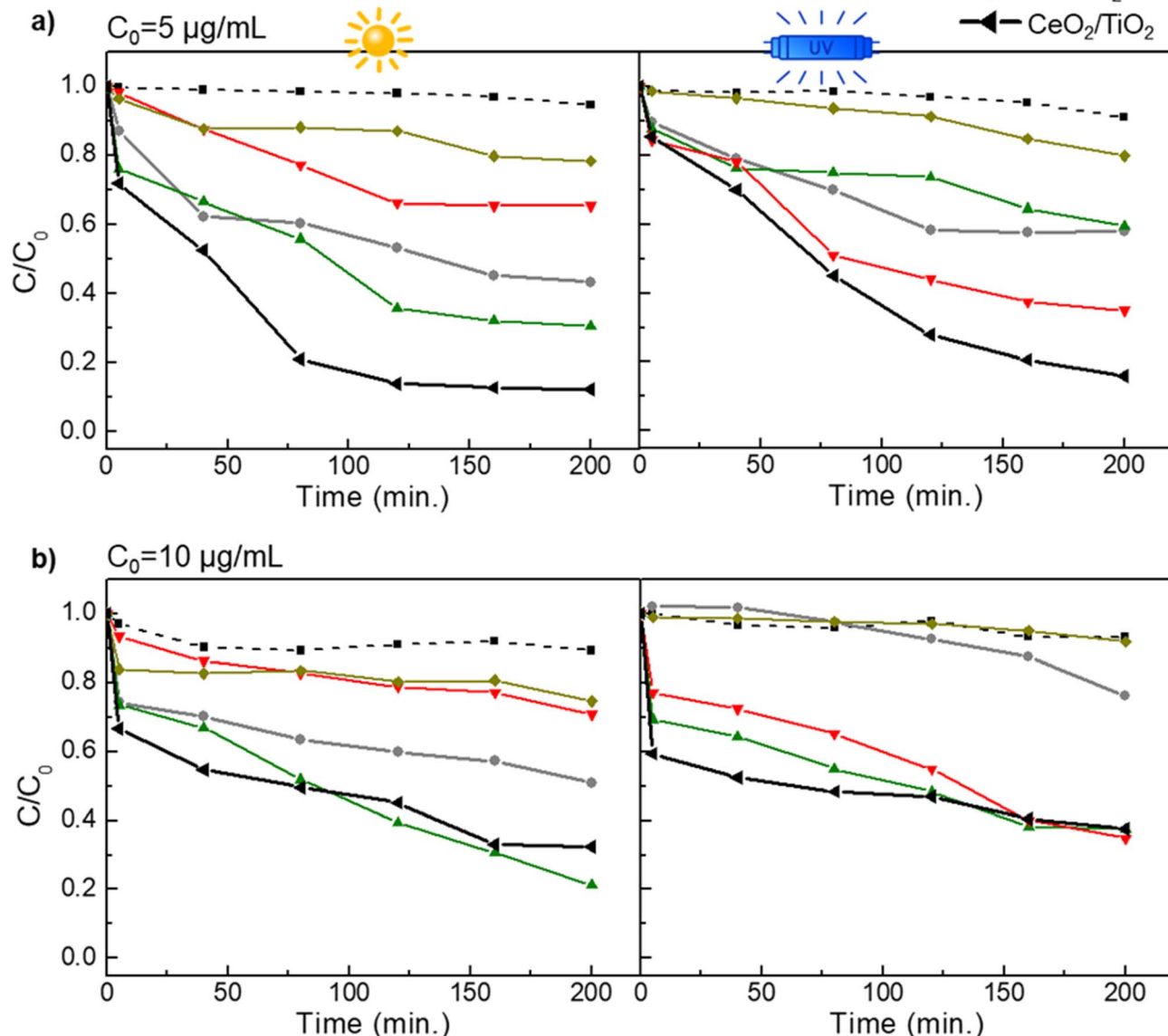


Fig. 6 Photocatalytic performance in the degradation of SMX of the hybrid  $\text{CeO}_2/\text{TiO}_2$ ,  $\text{Au}/\text{TiO}_2$  and single component NPs under visible and UV light. (a) SMX initial concentration of  $5 \mu\text{g mL}^{-1}$ ; (b) SMX initial concentration of  $10 \mu\text{g mL}^{-1}$ . Black and grey line correspond to  $\text{CeO}_2/\text{TiO}_2$  and  $\text{Au}/\text{TiO}_2$  hybrids respectively. Yellow line is  $\text{AuNPs}$ , green line is  $\text{CeO}_2\text{NPs}$ , red line is  $\text{TiO}_2\text{NPs}$  and dashed line correspond to the control ( $\text{H}_2\text{O}$ ). All photocatalysts were used at a concentration of  $0.5 \text{ mg mL}^{-1}$ . The control group (ctrl) consists of the antibiotic dissolved in a water solvent. The molecular structure of SMX is in Fig. S4.†

for the CIP degradation. Fig. 6 shows a similar pattern of SMX degradation as observed in the CIP degradation experiments.  $\text{CeO}_2/\text{TiO}_2$  exhibited superior and faster catalytic performance under UV and sun irradiation than other photocatalysts. Note that to achieve 100% SMX degradation, a lower concentration than in case of CIP degradation was needed (initial SMX concentrations of  $5 \mu\text{g L}^{-1}$  and  $10 \mu\text{g L}^{-1}$ ), probably due to the

different molecular structures of both antibiotics and that the system was optimized for CIP. Specifically, at  $\text{SMX } C_0 = 5 \mu\text{g mL}^{-1}$  and under sun irradiation,  $\text{CeO}_2/\text{TiO}_2$  showed the highest degradation (88%) followed by  $\text{CeO}_2\text{NPs}$  (70%) and  $\text{Au}/\text{TiO}_2$  (57%)  $\text{CeO}_2$  and  $\text{TiO}_2$  NPs (*c.a.* 35%). At  $\text{SMX } C_0 = 10 \mu\text{g mL}^{-1}$ , suggesting once again the importance of the  $\text{CeO}_2$  co-catalyst properties for photocatalytic reactions under visible light.

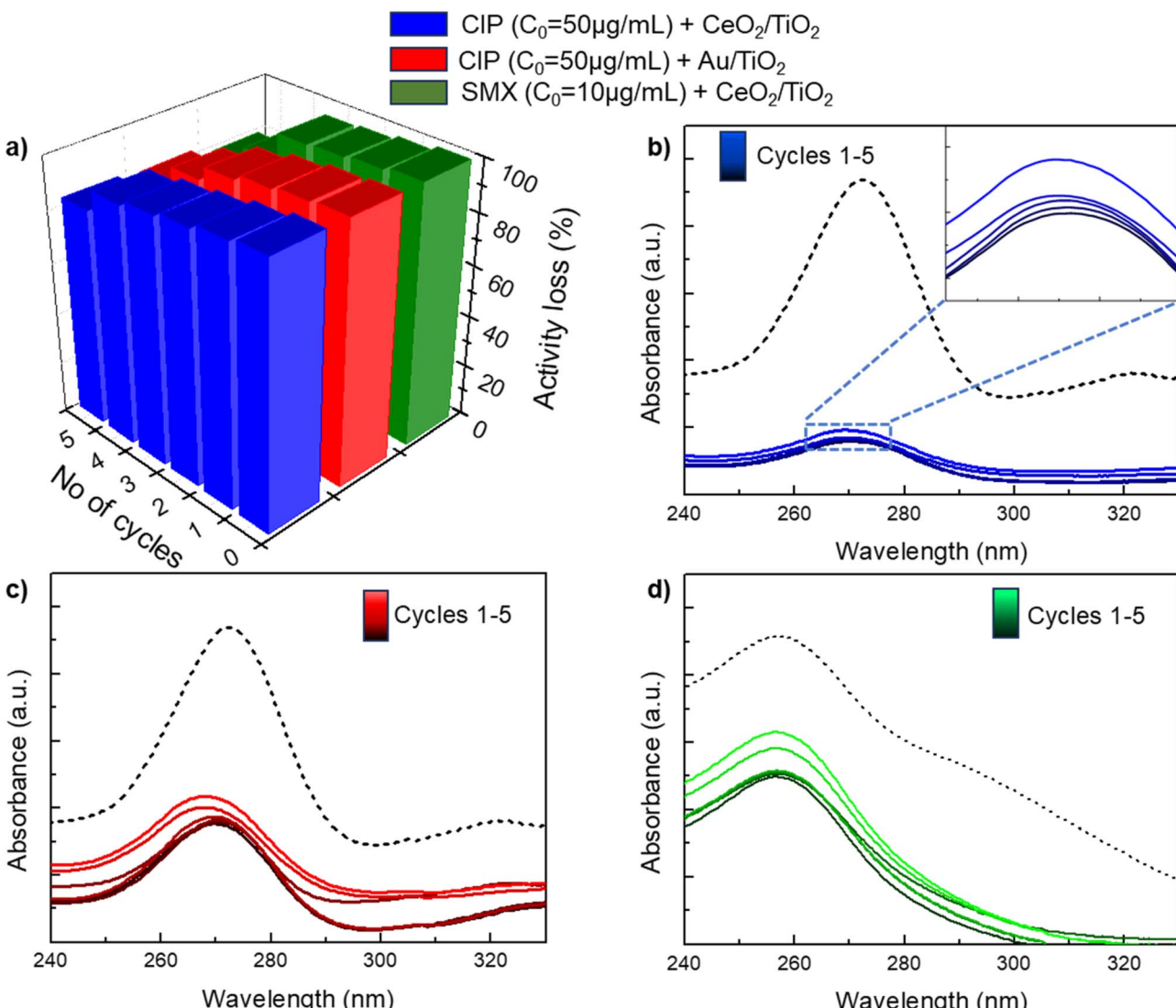


Fig. 7 Stability studies of the  $\text{CeO}_2/\text{TiO}_2$  and  $\text{Au}/\text{TiO}_2$  photocatalysts under sun irradiation. (a) Degradation of CIP or SMX at  $50\mu\text{g mL}^{-1}$  in different cycles of recovering the hybrids from the solution compared with the degradation showed by the as-synthesized hybrid nanocomposites. (b) UV-VIS absorbance of CIP (dashed line; peak at 272 nm) and with different cycles exposed to  $\text{CeO}_2/\text{TiO}_2$ . (c) UV-VIS absorbance of CIP and under the different cycles exposed to  $\text{Au}/\text{TiO}_2$ . (d) UV-VIS absorbance of SMX (dashed line; peak at 265 nm) and with different cycles exposed to  $\text{CeO}_2/\text{TiO}_2$ .

Interestingly, in a specific case, at the highest initial concentration of antibiotics ( $50\mu\text{g mL}^{-1}$  of CIP and  $10\mu\text{g mL}^{-1}$  of SMX),  $\text{CeO}_2$ NPs exhibited a higher rate of degradation compared to the  $\text{CeO}_2/\text{TiO}_2$  hybrids. It is important to note here that, even though the hybrids possess a greater surface area at the same mass concentration (Table S1†), in the experimental setup the single-component NPs have higher colloidal stability and, consequently, enhanced mobility in solution. This disparity in colloidal behaviour may account for the observed increase in catalytic activity.

In any case, the results altogether and the fact that  $\text{CeO}_2$  itself also showed efficient photocatalytic activity in the degradation of CIP, suggest the superior capability of  $\text{CeO}_2$  as a co-catalyst which can be attributed to its unique redox properties and its characteristic d and f electronic orbital

configurations,<sup>96-99</sup> along with other advantages such as the reported visible active band gap value, large oxygen storage capacity, and its variable oxidation states ( $\text{Ce}^{3+}$ ,  $\text{Ce}^{4+}$ ) which favor electron transfer and improve the electron-hole separation. This non-stoichiometry of  $\text{CeO}_2$  has also been related with its capacity to store oxygen and release them in oxidation reactions for *e.g.* the photocatalytic degradation of organic and pharmaceutical pollutants.<sup>97,100-102</sup> Apart from their inherent ability to initiate photocatalytic reactions by themselves, it has been reported that  $\text{Ce}^{4+}$  ions in the  $\text{CeO}_2$  crystal structure can easily capture photogenerated electrons and form  $\text{Ce}^{3+}$  ions, acting as an electron trapping agent and allowing to decrease the recombination rate of the photogenerated charges in the  $\text{TiO}_2$ .<sup>103</sup> In addition, this stored oxygen can also be transferred to  $\text{TiO}_2$ , which increases both the rate of oxygen reduction and



the efficacy of the electron-hole separation of  $\text{TiO}_2$ NPs (see schema in Fig. 3).<sup>104</sup>

### 3.4. Stability studies of the $\text{CeO}_2/\text{TiO}_2$ and $\text{Au}/\text{TiO}_2$ photocatalysts

The stability and reusability of newly developed photocatalysts is a key aspect to take into account for practical applications. In our experiments, the stability of the employed  $\text{CeO}_2/\text{TiO}_2$  and  $\text{Au}/\text{TiO}_2$  photocatalysts has been evaluated under sunlight for five consecutive cycles at the highest concentration of CIP/SMX used in the antibiotic degradation experiments. For each cycle, freshly prepared antibiotic solutions were used and  $\text{CeO}_2/\text{TiO}_2$  or  $\text{Au}/\text{TiO}_2$  were collected by centrifugation and drying the resulting pellet. Fig. 7 shows that the efficiency of CIP/SMX degradation remain stable for both photocatalysts during the first three cycles, but is reduced by *c.a.* 20% at the fifth cycle. This decrease in the degradation efficiency could be attributed to the consecutive drying and resuspension processes that may agglomerate the NPs resulting in a decrease in the available surface area for the catalytic reaction, since no leaching of metal in the supernatants after the washing cycle has been detected by ICP-MS.

## 4. Conclusions

Antibiotic residues in wastewaters are of particular concern due to their impact on marine and fluvial ecosystems and the development of antibiotic resistance. Different approaches have been proposed and used to remove antibiotics from water sources such as electrochemical methods, ozonation, reverse osmosis, membrane filtration, biological treatments and advanced oxidation. Among them, photocatalytic degradation using  $\text{TiO}_2$ -based nanomaterials has been widely explored in the last decades due to its high photocatalytic activity under UV light among other advantages such as its stability in a large range pH and its low-cost. To expand the  $\text{TiO}_2$  photocatalytic activity under sun light, a wide variety of photocatalysts based on doping  $\text{TiO}_2$  with metal ions or coupling it with light-active nanomaterials have been proposed, all with excellent results. In a typical study focusing on the photocatalytic degradation of pollutants using such nanomaterials, a photocatalyst is characterized and subsequently different parameters are modified to evaluate its activity. Herein, we aimed to evaluate and compare the photocatalytic degradation of CIP and SMX employing two different types of  $\text{TiO}_2$  hybrid nanomaterials, semiconductor  $\text{CeO}_2/\text{TiO}_2$  and metal  $\text{Au}/\text{TiO}_2$ , as representatives from two main families of novel photocatalysts proposed in previous scientific literature. Indeed, conducting a comprehensive comparison is a challenging task, as it involves numerous parameters related to co-catalyst characteristics, including size, shape, and addition ratio, among others. In this study, co-catalyst sizes ranging from 5 to 10 nanometers and a co-catalyst loading of 5% (at%) were employed. Both photocatalysts were extensively characterized by HR-TEM, XRD, UV-VIS, DLS, BET and XPS. The characterization showed that  $\text{CeO}_2/\text{TiO}_2$  and  $\text{Au}/\text{TiO}_2$  consisted of heterostructured

nanocomposites containing both single component NPs in the hybrid structure and showing a decrease of the  $E_g$  values (bandgap) with respect to pure  $\text{TiO}_2$ , allowing photocatalytic reaction to occur under sunlight.

The results of the antibiotic degradation showed that although both  $\text{CeO}_2/\text{TiO}_2$  and  $\text{Au}/\text{TiO}_2$  show enhanced photocatalytic activity under sun irradiation,  $\text{CeO}_2/\text{TiO}_2$  consistently exhibited the highest performance. These results suggest that the unique redox properties of  $\text{CeO}_2$ , as well as its characteristic electronic configuration and large oxygen storage capacity have a crucial role for the enhanced photocatalytic activity. Its particular electronic configuration allows  $\text{CeO}_2$  to act as an electron trapping agent, enabling both to participate in oxidation reactions by itself and to decrease the recombination rate of the photogenerated charges in  $\text{TiO}_2$ . In addition, both  $\text{TiO}_2$  and  $\text{CeO}_2$  are materials with high redox potential ( $\text{Ti}^{4+}/\text{Ti}^{3+}$  and  $\text{Ce}^{4+}/\text{Ce}^{3+}$ ) and their photocatalytic performance is boosted by their associated defects and oxygen vacancies, thus making  $\text{CeO}_2/\text{TiO}_2$  hybrid nanomaterials promising candidates for a range of environmental and energetic applications.

## Author contributions

M. Z. and E. C. conceptualized and designed the research. M. Z., S. J., J. T., and Y. Z. synthesized the photocatalysts and S. J., J. T., Y. L., X. L., and L. L. characterized them. M. Z., G. C., Z. J., and E. C. collected, processed and interpreted the data. M. Z., Z. J., and E. C. wrote the manuscript. All authors discussed the results, commented and reviewed the manuscript.

## Conflicts of interest

The authors declare no competing financial interest.

## Acknowledgements

The study was financially supported by the National Natural Science Foundation of China (22005221 to M. Z.), the Wuyi University (2018TP010 to E. C., 2018TP011 and 2020FKZX05 to M. Z.), and the Instituto de Salud Carlos III (PI19/00774 and BA22/00017 to G. C., co-funded by the European Regional Development Fund, European Union, “A way to make Europe”).

## References

- 1 X. Bai, W. Chen, B. Wang, T. Sun, B. Wu and Y. Wang, Photocatalytic Degradation of Some Typical Antibiotics: Recent Advances and Future Outlooks, *Int. J. Mol. Sci.*, 2022, **23**, 8130.
- 2 R. B. González-González, R. Parra-Saldívar, W. F. Alsanie and H. M. N. Iqbal, Nanohybrid catalysts with porous structures for environmental remediation through photocatalytic degradation of emerging pollutants, *Environ. Res.*, 2022, **214**, 113955.
- 3 F. Méndez-Arriaga, S. Esplugas and J. Giménez, Photocatalytic degradation of non-steroidal anti-



inflammatory drugs with TiO<sub>2</sub> and simulated solar irradiation, *Water Res.*, 2008, **42**, 585–594.

4 Z. Wei, J. Liu and W. Shangguan, A review on photocatalysis in antibiotic wastewater: Pollutant degradation and hydrogen production, *Chin. J. Catal.*, 2020, **41**, 1440–1450.

5 A. Fujishima, T. N. Rao and D. A. Tryk, Titanium dioxide photocatalysis, *J. Photochem. Photobiol. C*, 2000, **1**, 1–21.

6 M. R. Prairie, L. R. Evans, B. M. Stange and S. L. Martinez, An investigation of titanium dioxide photocatalysis for the treatment of water contaminated with metals and organic chemicals, *Environ. Sci. Technol.*, 1993, **27**, 1776–1782.

7 Y. Liu, Z. Li, M. Green, M. Just, Y. Y. Li and X. Chen, Titanium dioxide nanomaterials for photocatalysis, *J. Phys. D: Appl. Phys.*, 2017, **50**, 193003.

8 A. Fujishima and X. Zhang, Titanium dioxide photocatalysis: present situation and future approaches, *C. R. Chim.*, 2006, **9**, 750–760.

9 M. Anpo, Y. Ichihashi, M. Takeuchi and H. Yamashita, Design of unique titanium oxide photocatalysts by an advanced metal ion-implantation method and photocatalytic reactions under visible light irradiation, *Res. Chem. Intermed.*, 1998, **24**, 143–149.

10 M. Haruta, Size- and support-dependency in the catalysis of gold, *Catal. Today*, 1997, **36**, 153–166.

11 D. A. Panayotov, A. I. Frenkel and J. R. Morris, Catalysis and Photocatalysis by Nanoscale Au/TiO<sub>2</sub>: Perspectives for Renewable Energy, *ACS Energy Lett.*, 2017, **2**, 1223–1231.

12 Y. Tian and T. Tatsuma, Mechanisms and Applications of Plasmon-Induced Charge Separation at TiO<sub>2</sub> Films Loaded with Gold Nanoparticles, *J. Am. Chem. Soc.*, 2005, **127**, 7632–7637.

13 N. Zhang, S. Liu, X. Fu and Y.-J. Xu, Synthesis of M@TiO<sub>2</sub> (M = Au, Pd, Pt) Core-Shell Nanoconposites with Tunable Photoreactivity, *J. Phys. Chem. C*, 2011, **115**, 9136–9145.

14 L. Li, W. Ouyang, Z. Zheng, K. Ye, Y. Guo, Y. Qin, Z. Wu, Z. Lin, T. Wang and S. Zhang, Synergetic photocatalytic and thermocatalytic reforming of methanol for hydrogen production based on Pt@TiO<sub>2</sub> catalyst, *Chin. J. Catal.*, 2022, **43**, 1258–1266.

15 S. Pany, B. Naik, S. Martha and K. Parida, Plasmon Induced Nano Au Particle Decorated over S,N-Modified TiO<sub>2</sub> for Exceptional Photocatalytic Hydrogen Evolution under Visible Light, *ACS Appl. Mater. Interfaces*, 2014, **6**, 839–846.

16 K. Dong, J. He, J. Liu, F. Li, L. Yu, Y. Zhang, X. Zhou and H. Ma, Photocatalytic performance of Cu<sub>2</sub>O-loaded TiO<sub>2</sub>/rGO nanoheterojunctions obtained by UV reduction, *J. Mater. Sci.*, 2017, **52**, 6754–6766.

17 M. L. A. Kumari, L. G. Devi, G. Maia, T.-W. Chen, N. Al-Zaqri and M. A. Ali, Mechanochemical synthesis of ternary heterojunctions TiO<sub>2</sub>(A)/TiO<sub>2</sub>(R)/ZnO and TiO<sub>2</sub>(A)/TiO<sub>2</sub>(R)/SnO<sub>2</sub> for effective charge separation in semiconductor photocatalysis: A comparative study, *Environ. Res.*, 2022, **203**, 111841.

18 J. A. Pinedo-Escobar, J. Fan, E. Moctezuma, C. Gomez-Solís, C. J. Carrillo Martinez and E. Gracia-Espino, Nanoparticulate Double-Heterojunction Photocatalysts Comprising TiO<sub>2</sub>(Anatase)/WO<sub>3</sub>/TiO<sub>2</sub>(Rutile) with Enhanced Photocatalytic Activity toward the Degradation of Methyl Orange under Near-Ultraviolet and Visible Light, *ACS Omega*, 2021, **6**, 11840–11848.

19 R. B. Rajput, S. N. Jamble and R. B. Kale, A review on TiO<sub>2</sub>/SnO<sub>2</sub> heterostructures as a photocatalyst for the degradation of dyes and organic pollutants, *J. Environ. Manage.*, 2022, **307**, 114533.

20 N. Zhang, S. Liu and Y.-J. Xu, Recent progress on metal core@semiconductor shell nanocomposites as a promising type of photocatalyst, *Nanoscale*, 2012, **4**, 2227–2238.

21 Y. Chen, G. Mao, Y. Tang, H. Wu, G. Wang, L. Zhang and Q. Liu, Synthesis of core-shell nanostructured Cr<sub>2</sub>O<sub>3</sub>/C@TiO<sub>2</sub> for photocatalytic hydrogen production, *Chin. J. Catal.*, 2021, **42**, 225–234.

22 Z. Bian, T. Tachikawa, P. Zhang, M. Fujitsuka and T. Majima, Au/TiO<sub>2</sub> Superstructure-Based Plasmonic Photocatalysts Exhibiting Efficient Charge Separation and Unprecedented Activity, *J. Am. Chem. Soc.*, 2014, **136**, 458–465.

23 R. Jiang, B. Li, C. Fang and J. Wang, Metal/Semiconductor Hybrid Nanostructures for Plasmon-Enhanced Applications, *Adv. Mater.*, 2014, **26**, 5274–5309.

24 S. Pany and K. M. Parida, A facile in situ approach to fabricate N,S-TiO<sub>2</sub>/g-C<sub>3</sub>N<sub>4</sub> nanocomposite with excellent activity for visible light induced water splitting for hydrogen evolution, *Phys. Chem. Chem. Phys.*, 2015, **17**, 8070–8077.

25 K. M. Parida, S. Pany and B. Naik, Green synthesis of fibrous hierarchical meso-macroporous N doped TiO<sub>2</sub> nanophotocatalyst with enhanced photocatalytic H<sub>2</sub> production, *Int. J. Hydrogen Energy*, 2013, **38**, 3545–3553.

26 A. Ayati, A. Ahmadpour, F. F. Bamoharram, B. Tanhaei, M. Mänttäri and M. Sillanpää, A review on catalytic applications of Au/TiO<sub>2</sub> nanoparticles in the removal of water pollutant, *Chemosphere*, 2014, **107**, 163–174.

27 E. Kowalska, R. Abe and B. Ohtani, Visible light-induced photocatalytic reaction of gold-modified titanium(iv) oxide particles: action spectrum analysis, *Chem. Commun.*, 2009, 241–243, DOI: [10.1039/B815679D](https://doi.org/10.1039/B815679D).

28 M.-I. Mendoza-Diaz, J. Cure, M. D. Rouhani, K. Tan, S.-G. Patnaik, D. Pech, M. Quevedo-Lopez, T. Hungria, C. Rossi and A. Estève, On the UV–Visible Light Synergetic Mechanisms in Au/TiO<sub>2</sub> Hybrid Model Nanostructures Achieving Photoreduction of Water, *J. Phys. Chem. C*, 2020, **124**, 25421–25430.

29 D. Widmann and R. J. Behm, Activation of molecular oxygen and the nature of the active oxygen species for CO oxidation on oxide supported Au catalysts, *Acc. Chem. Res.*, 2014, **47**, 740–749.

30 M. Chen, K. Luo, D. Kumar, W. T. Wallace, C. W. Yi, K. K. Gath and D. W. Goodman, The structure of ordered Au films on TiO<sub>x</sub>, *Surf. Sci.*, 2007, **601**, 632–637.

31 M. S. Chen and D. W. Goodman, Structure–activity relationships in supported Au catalysts, *Catal. Today*, 2006, **111**, 22–33.



32 Y. Maeda, Y. Iizuka and M. Kohyama, Generation of Oxygen Vacancies at a Au/TiO<sub>2</sub> Perimeter Interface during CO Oxidation Detected by in Situ Electrical Conductance Measurement, *J. Am. Chem. Soc.*, 2013, **135**, 906–909.

33 Y. Feng, P. Ma, Z. Wang, Y. Shi, Z. Wang, Y. Peng, L. Jing, Y. Liu, X. Yu, X. Wang, X. Zhang, J. Deng and H. Dai, Synergistic Effect of Reactive Oxygen Species in Photothermocatalytic Removal of VOCs from Cooking Oil Fumes over Pt/CeO<sub>2</sub>/TiO<sub>2</sub>, *Environ. Sci. Technol.*, 2022, **56**, 17341–17351.

34 L. Gnanasekaran, S. Rajendran, A. K. Priya, D. Durgalakshmi, D.-V. N. Vo, L. Cornejo-Ponce, F. Gracia and M. Soto-Moscoso, Photocatalytic degradation of 2,4-dichlorophenol using bio-green assisted TiO<sub>2</sub>-CeO<sub>2</sub> nanocomposite system, *Environ. Res.*, 2021, **195**, 110852.

35 J. Tian, Y. Sang, Z. Zhao, W. Zhou, D. Wang, X. Kang, H. Liu, J. Wang, S. Chen, H. Cai and H. Huang, Enhanced Photocatalytic Performances of CeO<sub>2</sub>/TiO<sub>2</sub> Nanobel Heterostructures, *Small*, 2013, **9**, 3864–3872.

36 J. Wang, F. Meng, W. Xie, C. Gao, Y. Zha, D. Liu and P. Wang, TiO<sub>2</sub>/CeO<sub>2</sub> composite catalysts: synthesis, characterization and mechanism analysis, *Appl. Phys. A*, 2018, **124**, 1–6.

37 H. Eskandarloo, A. Badiei and M. A. Behnajady, TiO<sub>2</sub>/CeO<sub>2</sub> Hybrid Photocatalyst with Enhanced Photocatalytic Activity: Optimization of Synthesis Variables, *Ind. Eng. Chem. Res.*, 2014, **53**, 7847–7855.

38 B. C. Steimle, J. L. Fenton and R. E. Schaak, Rational construction of a scalable heterostructured nanorod megalibrary, *Science*, 2020, **367**, 418–424.

39 D. G. J. Larsson, C. de Pedro and N. Paxeus, Effluent from drug manufactures contains extremely high levels of pharmaceuticals, *J. Hazard. Mater.*, 2007, **148**, 751–755.

40 J. Fick, H. Söderström, R. H. Lindberg, C. Phan, M. Tysklind and D. G. J. Larsson, Contamination of surface, ground, and drinking water from pharmaceutical production, *Environ. Toxicol. Chem.*, 2009, **28**, 2522–2527.

41 J. Bengtsson-Palme and D. G. J. Larsson, Concentrations of antibiotics predicted to select for resistant bacteria: proposed limits for environmental regulation, *Environ. Int.*, 2016, **86**, 140–149.

42 [https://www.amrindustryalliance.org/wp-content/uploads/2018/09/AMR\\_Industry\\_Alliance\\_List-of-Predicted-No-Effect-Concentrations-PNECs.pdf](https://www.amrindustryalliance.org/wp-content/uploads/2018/09/AMR_Industry_Alliance_List-of-Predicted-No-Effect-Concentrations-PNECs.pdf), [https://www.amrindustryalliance.org/wp-content/uploads/2018/09/AMR\\_Industry\\_Alliance\\_List-of-Predicted-No-Effect-Concentrations-PNECs.pdf](https://www.amrindustryalliance.org/wp-content/uploads/2018/09/AMR_Industry_Alliance_List-of-Predicted-No-Effect-Concentrations-PNECs.pdf), accessed May, 13, 2023.

43 G. Prasannamedha and P. S. Kumar, A review on contamination and removal of sulfamethoxazole from aqueous solution using cleaner techniques: present and future perspective, *J. Cleaner Prod.*, 2020, **250**, 119553.

44 J. O. Straub, Aquatic environmental risk assessment for human use of the old antibiotic sulfamethoxazole in Europe, *Environ. Toxicol. Chem.*, 2016, **35**, 767–779.

45 N. R. Jana, L. Gearheart and C. J. Murphy, Seeding Growth for Size Control of 5–40 nm Diameter Gold Nanoparticles, *Langmuir*, 2001, **17**, 6782–6786.

46 M. Zeng, Y. Shu, M. Parra-Robert, D. Desai, H. Zhou, Q. Li, Z. Rong, D. S. Karaman, H. Yang, J. Peng, G. Fernandez-Varo, W. Jiménez, G. Casals, V. Puntes, J. M. Rosenholm and E. Casals, Scalable synthesis of multicomponent multifunctional inorganic core@mesoporous silica shell nanocomposites, *Mater. Sci. Eng. C*, 2021, **128**, 112272.

47 A. Pottier, S. Cassaignon, C. Chanéac, F. Villain, E. Tronc and J.-P. Jolivet, Size tailoring of TiO<sub>2</sub> anatase nanoparticles in aqueous medium and synthesis of nanocomposites. Characterization by Raman spectroscopy, *J. Mater. Chem.*, 2003, **13**, 877–882.

48 M. Manasa, P. R. Chandewar and H. Mahalingam, Photocatalytic degradation of ciprofloxacin & norfloxacin and disinfection studies under solar light using boron & cerium doped TiO<sub>2</sub> catalysts synthesized by green EDTA-citrate method, *Catal. Today*, 2021, **375**, 522–536.

49 H. Wang, J. Li, C. Ma, Q. Guan, Z. Lu, P. Huo and Y. Yan, Melamine modified P25 with heating method and enhanced the photocatalytic activity on degradation of ciprofloxacin, *Appl. Surf. Sci.*, 2015, **329**, 17–22.

50 A. García, L. Delgado, J. A. Torà, E. Casals, E. González, V. Puntes, X. Font, J. Carrera and A. Sánchez, Effect of cerium dioxide, titanium dioxide, silver, and gold nanoparticles on the activity of microbial communities intended in wastewater treatment, *J. Hazard. Mater.*, 2012, **199–200**, 64–72.

51 E. Casals, E. Gonzalez and V. F. Puntes, Reactivity of inorganic nanoparticles in biological environments: insights into nanotoxicity mechanisms, *J. Phys. D: Appl. Phys.*, 2012, **45**, 443001.

52 E. Casals, M. Zeng, M. Parra-Robert, G. Fernández-Varo, M. Morales-Ruiz, W. Jiménez, V. Puntes and G. Casals, Cerium Oxide Nanoparticles: Advances in Biodistribution, Toxicity, and Preclinical Exploration, *Small*, 2020, **16**, 1907322.

53 D. T. Thompson, Using gold nanoparticles for catalysis, *Nano Today*, 2007, **2**, 40–43.

54 M. Parra-Robert, E. Casals, N. Massana, M. Zeng, M. Perramón, G. Fernández-Varo, M. Morales-Ruiz, V. Puntes, W. Jiménez and G. Casals, Beyond the Scavenging of Reactive Oxygen Species (ROS): Direct Effect of Cerium Oxide Nanoparticles in Reducing Fatty Acids Content in an In Vitro Model of Hepatocellular Steatosis, *Biomolecules*, 2019, **9**, 425.

55 L. S. R. Rocha, A. Z. Simões, C. Macchi, A. Somoza, G. Giulietti, M. A. Ponce and E. Longo, Synthesis and defect characterization of hybrid ceria nanostructures as a possible novel therapeutic material towards COVID-19 mitigation, *Sci. Rep.*, 2022, **12**, 3341.

56 O. Zuas and N. Hamim, Synthesis, Characterization and Properties of CeO<sub>2</sub>-doped TiO<sub>2</sub> Composite Nanocrystals, *Mater. Sci.*, 2013, **19**, 443–447.

57 Y. Li, W. Li, F. Liu, M. Li, X. Qi, M. Xue, Y. Wang and F. Han, Construction of CeO<sub>2</sub>/TiO<sub>2</sub> heterojunctions immobilized on activated carbon fiber and its synergistic effect between adsorption and photodegradation for toluene removal, *J. Nanopart. Res.*, 2020, **22**, 122.



58 M. Wang, J. Ioccozia, L. Sun, C. Lin and Z. Lin, Inorganic-modified semiconductor TiO<sub>2</sub> nanotube arrays for photocatalysis, *Energy Environ. Sci.*, 2014, **7**, 2182–2202.

59 U. Balachandran and N. G. Eror, Raman spectra of titanium dioxide, *J. Solid State Chem.*, 1982, **42**, 276–282.

60 V. Swamy, A. Kuznetsov, L. S. Dubrovinsky, P. F. McMillan, V. B. Prakapenka, G. Shen and B. C. Muddle, Size-Dependent Pressure-Induced Amorphization in Nanoscale  $\text{TiO}_2$ , *Phys. Rev. Lett.*, 2006, **96**, 135702.

61 S. Pany and K. M. Parida, Sulfate-Anchored Hierarchical Meso-Macroporous N-doped TiO<sub>2</sub>: A Novel Photocatalyst for Visible Light H<sub>2</sub> Evolution, *ACS Sustain. Chem. Eng.*, 2014, **2**, 1429–1438.

62 H. Abdullah, M. R. Khan, M. Pudukudy, Z. Yaakob and N. A. Ismail, CeO<sub>2</sub>-TiO<sub>2</sub> as a visible light active catalyst for the photoreduction of CO<sub>2</sub> to methanol, *J. Rare Earths*, 2015, **33**, 1155–1161.

63 N. Aman, P. K. Satapathy, T. Mishra, M. Mahato and N. N. Das, Synthesis and photocatalytic activity of mesoporous cerium doped TiO<sub>2</sub> as visible light sensitive photocatalyst, *Mater. Res. Bull.*, 2012, **47**, 179–183.

64 Z. Fan, F. Meng, J. Gong, H. Li, Y. Hu and D. Liu, Enhanced photocatalytic activity of hierarchical flower-like CeO<sub>2</sub>/TiO<sub>2</sub> heterostructures, *Mater. Lett.*, 2016, **175**, 36–39.

65 G. Vieira, H. José, M. Peterson, V. Baldissarelli, P. Alvarez and R. Moreira, CeO<sub>2</sub>/TiO<sub>2</sub> nanostructures enhance adsorption and photocatalytic degradation of organic compounds in aqueous suspension, *J. Photochem. Photobiol. A*, 2017, **353**, 325–336.

66 H. Li, G. Wang, F. Zhang, Y. Cai, Y. Wang and I. Djerdj, Surfactant-assisted synthesis of CeO<sub>2</sub> nanoparticles and their application in wastewater treatment, *RSC Adv.*, 2012, **2**, 12413–12423.

67 J. B. Coulter and D. P. Birnie III, Assessing Tauc Plot Slope Quantification: ZnO Thin Films as a Model System, *Phys. Status Solidi B*, 2018, **255**, 1700393.

68 J. Tauc, R. Grigorovici and A. Vancu, Optical Properties and Electronic Structure of Amorphous Germanium, *Phys. Status Solidi B*, 1966, **15**, 627–637.

69 E. A. Davis and N. F. Mott, Conduction in non-crystalline systems V. Conductivity, optical absorption and photoconductivity in amorphous semiconductors, *Philos. Mag. A*, 1970, **22**, 0903–0922.

70 J. Klein, L. Kampermann, B. Mockenhaupt, M. Behrens, J. Strunk and G. Bacher, Limitations of the Tauc Plot Method, *Adv. Funct. Mater.*, 2023, 2304523.

71 S. Ameen, M. Shaheer Akhtar, H.-K. Seo and H.-S. Shin, Solution-processed CeO<sub>2</sub>/TiO<sub>2</sub> nanocomposite as potent visible light photocatalyst for the degradation of bromophenol dye, *Chem. Eng. J.*, 2014, **247**, 193–198.

72 H. Sun, Q. He, P. She, S. Zeng, K. Xu, J. Li, S. Liang and Z. Liu, One-pot synthesis of Au@TiO<sub>2</sub> yolk-shell nanoparticles with enhanced photocatalytic activity under visible light, *J. Colloid Interface Sci.*, 2017, **505**, 884–891.

73 R. Jaiswal, N. Patel, A. Dashora, R. Fernandes, M. Yadav, R. Edla, R. S. Varma, D. C. Kothari, B. L. Ahuja and A. Miotello, Efficient Co-B-codoped TiO<sub>2</sub> photocatalyst for degradation of organic water pollutant under visible light, *Appl. Catal., B*, 2016, **183**, 242–253.

74 R. Shetty, V. B. Chavan, P. S. Kulkarni, B. D. Kulkarni and S. P. Kamble, Photocatalytic Degradation of Pharmaceuticals Pollutants Using N-Doped TiO<sub>2</sub> Photocatalyst: Identification of CFX Degradation Intermediates, *Indian Chem. Eng.*, 2017, **59**, 177–199.

75 M. N. Abellán, B. Bayarri, J. Giménez and J. Costa, Photocatalytic Degradation of Sulfamethoxazole in Aqueous Suspension of TiO<sub>2</sub>, *Appl. Catal., B*, 2007, **74**, 233–241.

76 E. Borowska, J. F. Gomes, R. C. Martins, R. M. Quinta-Ferreira, H. Horn and M. Gmurek, Solar Photocatalytic Degradation of Sulfamethoxazole by TiO<sub>2</sub> Modified with Noble Metals, *Catalysts*, 2019, **9**, 500.

77 J. C. Durán-Álvarez, E. Avella, R. M. Ramírez-Zamora and R. Zanella, Photocatalytic degradation of ciprofloxacin using mono- (Au, Ag and Cu) and bi- (Au-Ag and Au-Cu) metallic nanoparticles supported on TiO<sub>2</sub> under UV-C and simulated sunlight, *Catal. Today*, 2016, **266**, 175–187.

78 X. Zheng, S. Xu, Y. Wang, X. Sun, Y. Gao and B. Gao, Enhanced degradation of ciprofloxacin by graphitized mesoporous carbon (GMC)-TiO<sub>2</sub> nanocomposite: strong synergy of adsorption-photocatalysis and antibiotics degradation mechanism, *J. Colloid Interface Sci.*, 2018, **527**, 202–213.

79 H. Gong and W. Chu, Determination and toxicity evaluation of the generated products in sulfamethoxazole degradation by UV/CoFe<sub>2</sub>O<sub>4</sub>/TiO<sub>2</sub>, *J. Hazard. Mater.*, 2016, **314**, 197–203.

80 S. P. Pattnaik, A. Behera, S. Martha, R. Acharya and K. Parida, Facile synthesis of exfoliated graphitic carbon nitride for photocatalytic degradation of ciprofloxacin under solar irradiation, *J. Mater. Sci.*, 2019, **54**, 5726–5742.

81 X. Yu, J. Zhang, J. Zhang, J. Niu, J. Zhao, Y. Wei and B. Yao, Photocatalytic degradation of ciprofloxacin using Zn-doped Cu<sub>2</sub>O particles: analysis of degradation pathways and intermediates, *Chem. Eng. J.*, 2019, **374**, 316–327.

82 T. A. Gad-Allah, M. E. Ali and M. I. Badawy, Photocatalytic oxidation of ciprofloxacin under simulated sunlight, *J. Hazard. Mater.*, 2011, **186**, 751–755.

83 Y. Yan, X. Liu, W. Fan, P. Lv and W. Shi, InVO<sub>4</sub> microspheres: preparation, characterization and visible-light-driven photocatalytic activities, *Chem. Eng. J.*, 2012, **200–202**, 310–316.

84 T. An, H. Yang, G. Li, W. Song, W. J. Cooper and X. Nie, Kinetics and mechanism of advanced oxidation processes (AOPs) in degradation of ciprofloxacin in water, *Appl. Catal., B*, 2010, **94**, 288–294.

85 M. Malakootian, A. Nasiri and M. Amiri Gharaghani, Photocatalytic degradation of ciprofloxacin antibiotic by TiO<sub>2</sub> nanoparticles immobilized on a glass plate, *Chem. Eng. Commun.*, 2020, **207**, 56–72.

86 A. Salma, S. Thoré-Bovleth, T. C. Schmidt and J. Tuerk, Dependence of transformation product formation on pH during photolytic and photocatalytic degradation of ciprofloxacin, *J. Hazard. Mater.*, 2016, **313**, 49–59.



87 F. Zheng, P. M. Martins, J. M. Queirós, C. J. Tavares, J. L. Vilas-Vilela, S. Lanceros-Méndez and J. Reguera, Size Effect in Hybrid TiO<sub>2</sub>:Au Nanostars for Photocatalytic Water Remediation Applications, *Int. J. Mol. Sci.*, 2022, **23**, 13741.

88 S. Krishnan and A. Shriwastav, Chlorophyll sensitized and salicylic acid functionalized TiO<sub>2</sub> nanoparticles as a stable and efficient catalyst for the photocatalytic degradation of ciprofloxacin with visible light, *Environ. Res.*, 2023, **216**, 114568.

89 L. Li, J. Liu, J. Zeng, J. Li, Y. Liu, X. Sun, L. Xu and L. Li, Complete Degradation and Detoxification of Ciprofloxacin by a Micro-/Nanostructured Biogenic Mn Oxide Composite from a Highly Active Mn(2+)-Oxidizing *Pseudomonas* Strain, *Nanomaterials*, 2021, **11**, 1660.

90 W. Shi, Y. Yan, Microwave-assisted synthesis of nano-scale BiVO<sub>4</sub> photocatalysts and their excellent visible-light-driven photocatalytic activity for the degradation of ciprofloxacin, *Chem. Eng. J.*, 2013, **215–216**, 740–746.

91 P. Huo, M. Zhou, Y. Tang, X. Liu, C. Ma, L. Yu and Y. Yan, Incorporation of N-ZnO/CdS/Graphene oxide composite photocatalyst for enhanced photocatalytic activity under visible light, *J. Alloys Compd.*, 2016, **670**, 198–209.

92 J. Yao, Z. Gao, Q. Meng, G. He and H. Chen, One-step synthesis of reduced graphene oxide based ceric dioxide modified with cadmium sulfide (CeO<sub>2</sub>/CdS/RGO) heterojunction with enhanced sunlight-driven photocatalytic activity, *J. Colloid Interface Sci.*, 2021, **594**, 621–634.

93 M. Yan, F. Zhu, W. Gu, L. Sun, W. Shi and Y. Hua, Construction of nitrogen-doped graphene quantum dots-BiVO<sub>4</sub>/g-C<sub>3</sub>N<sub>4</sub> Z-scheme photocatalyst and enhanced photocatalytic degradation of antibiotics under visible light, *RSC Adv.*, 2016, **6**, 61162–61174.

94 L. Wolski, K. Grzelak, M. Muńko, M. Frankowski, T. Grzyb and G. Nowaczyk, Insight into photocatalytic degradation of ciprofloxacin over CeO<sub>2</sub>/ZnO nanocomposites: unravelling the synergy between the metal oxides and analysis of reaction pathways, *Appl. Surf. Sci.*, 2021, **563**, 150338.

95 Y. Yan, S. Sun, Y. Song, X. Yan, W. Guan, X. Liu and W. Shi, Microwave-assisted in situ synthesis of reduced graphene oxide-BiVO<sub>4</sub> composite photocatalysts and their enhanced photocatalytic performance for the degradation of ciprofloxacin, *J. Hazard. Mater.*, 2013, **250–251**, 106–114.

96 J.-D. Cafun, K. O. Kvashnina, E. Casals, V. F. Puntes and P. Glatzel, Absence of Ce<sup>3+</sup> Sites in Chemically Active Colloidal Ceria Nanoparticles, *ACS Nano*, 2013, **7**, 10726–10732.

97 C. T. Campbell and C. H. F. Peden, Oxygen Vacancies and Catalysis on Ceria Surfaces, *Science*, 2005, **309**, 713–714.

98 F. Esch, S. Fabris, L. Zhou, T. Montini, C. Africh, P. Fornasiero, G. Comelli and R. Rosei, Electron Localization Determines Defect Formation on Ceria Substrates, *Science*, 2005, **309**, 752–755.

99 M. Nolan, S. C. Parker and G. W. Watson, The electronic structure of oxygen vacancy defects at the low index surfaces of ceria, *Surf. Sci.*, 2005, **595**, 223–232.

100 E. G. Heckert, S. Seal and W. T. Self, Fenton-Like Reaction Catalyzed by the Rare Earth Inner Transition Metal Cerium, *Environ. Sci. Technol.*, 2008, **42**, 5014–5019.

101 J. F. Jerratsch, X. Shao, N. Nilius, H. J. Freund, C. Popa, M. V. Ganduglia-Pirovano, A. M. Burow and J. Sauer, Electron localization in defective ceria films: a study with scanning-tunneling microscopy and density-functional theory, *Phys. Rev. Lett.*, 2011, **106**, 246801.

102 H. C. Yao and Y. F. Y. Yao, Ceria in automotive exhaust catalysts: I. Oxygen storage, *J. Catal.*, 1984, **86**, 254–265.

103 B. Jiang, S. Zhang, X. Guo, B. Jin and Y. Tian, Preparation and photocatalytic activity of CeO<sub>2</sub>/TiO<sub>2</sub> interface composite film, *Appl. Surf. Sci.*, 2009, **255**, 5975–5978.

104 V. Kumari, A. Sharma, N. Kumar, M. Sillanpää, P. R. Makgwane, M. Ahmaruzzaman, A. Hosseini-Bandegharaei, M. Rani and P. Chinnamuthu, TiO<sub>2</sub>-CeO<sub>2</sub> assisted heterostructures for photocatalytic mitigation of environmental pollutants: a comprehensive study on band gap engineering and mechanistic aspects, *Inorg. Chem. Commun.*, 2023, **151**, 110564.

